MEASURING ANGULAR RATE OF CELESTIAL OBJECTS USING THE SPACE SURVEILLANCE TELESCOPE

THESIS

Anthony J. Sligar, Captain, USAF

AFIT-ENG-MS-15-M-019

DEPARTMENT OF THE AIR FORCE
AIR UNIVERSITY

AIR FORCE INSTITUTE OF TECHNOLOGY

Wright-Patterson Air Force Base, Ohio

AFIT-ENG-MS-15-M-019

MEASURING ANGULAR RATE OF CELESTIAL OBJECTS USING THE SPACE

SURVEILLANCE TELESCOPE

THESIS

Presented to the Faculty

Department of Electrical and Computer Engineering

Graduate School of Engineering and Management

Air Force Institute of Technology

Air University

Air Education and Training Command

in Partial Fulfillment of the Requirements for the

Degree of Master of Science in Electrical Engineering

Anthony J. Sligar, B.S.E.E.

Captain, USAF

March 2015

AFIT-ENG-MS-15-M-019

MEASURING ANGULAR RATE OF CELESTIAL OBJECTS USING THE SPACE

SURVEILLANCE TELESCOPE

Anthony J. Sligar, B.S.E.E.
Captain, USAF

Committee Membership:

Stephen C. Cain, PhD
Chair

Lt Col Travis F. Blake, PhD
Member

Maj Milo W. Hyde, PhD
Member

AFIT-ENG-MS-15-M-019

Abstract

To date, much effort has been spent on improving the detection of space objects; however, the ability to track and catalogue space objects remains only as good as the ability to determine the object's position and angular rate. The foundation of space situational awareness (SSA) is the ability to detect a space object and to predict its location in the future. In order to accomplish SSA for Geosynchronous Earth Orbit (GEO) space objects, the Defense Advanced Research Projects Agency (DARPA) developed the Space Surveillance Telescope (SST) to enable ground-based, broad-area search, detection and tracking of small GEO objects in space. In general, the SST tracks along the sky at the sidereal rate where the stars will appear to be stationary, while objects within space not moving at this rate will appear to move across the focal array from data frame to data frame. As the time between each frame is known and the position of the detected object can be determined in the focal array, it is possible to measure the angular position and angular rate of a detected object. The two main types of detection algorithms used in this thesis are the binary hypothesis test (BHT) and the multi-hypothesis test (MHT), which both rely on a log-likelihood ratio (LLR); however, the MHT algorithm adds an additional step to correlate nine system point spread functions, or hypotheses, with the image data. These detection algorithms lead to varying degrees of accuracy and precision in determining the position and angular rate for a detected space object. The research within this thesis shows that the MHT algorithm is more accurate and precise than the BHT algorithm.

Acknowledgments

I would like to thank my fellow students in my electro-optics classes for helping me get through all the optics classes we have taken together. I would also like to show my appreciation to my advisor, Dr. Cain, for his continued patience and guidance in helping me understand and learn about optics and for helping me get through the thesis writing process.

Anthony J. Sligar

Table of Contents

List of Figures

List of Tables

List of Acronyms

Acronym   Definition

BHT Binary Hypothesis Test

CCD Charge-Coupled Device

CoI Center of Intensity

CoS Center of SNR

DARPA Defence Advanced Research Projects Agency

DoD Department of Defense

EO electro-optics

LLE Log-Likelihood Equation

LLR Log-Likelihood Ratio

LRT Likelihood Ratio Test

MHT Multi-Hypothesis Test

MHTOR Multi-Hypothesis Test with Outlier Removal

NEAs Near Earth Asteroids

NASA National Aeronautics and Space Administration

OTF Optical Transfer Function

PSF Point Spread Function

Acronym   Definition

SNR Signal to Noise Ratio

SSA Space Situational Awareness

SST Space Surveillance Telescope

MEASURING ANGULAR RATE OF CELESTIAL OBJECTS USING THE SPACE
SURVEILLANCE TELESCOPE

I. Introduction

1.1   Space Situational Awareness

Since the launch of Sputnik in 1957, the need for Space Situational Awareness (SSA) has become an ever more important task in conducting space operations [17]. SSA is predominantly concerned with characterizing and tracking human-created objects in Earth orbit. In its most basic sense, SSA is the ability to detect a space object and predict its location in the future; this data is known as the metric data of an Earth orbiting object [17]. In addition to the metric data, SSA seeks to characterize objects in space and the space environment.

In order to perform SSA using electro-optics systems, three steps must occur in sequential order: 1) the detection of an Earth orbiting object, 2) the determination of the object's angular position and rate, and 3) the steps to determine the object's orbit (orbital determination) from the calculated angular position and rate data. The detection of an Earth orbiting object has traditionally been done with three main types of sensors: ground-based radar, ground-based electro-optics (EO), and space-based sensors [17]. In order to improve SSA, the detection of an object must be accompanied by at least some degree of position information on that object.

The detection of Near Earth Asteroids (NEAs) is another important activity that ground-based electro-optics are used for. While not technically part of SSA, the detection techniques used to detect satellites and other man-made debris for SSA are nearly identical.

1

1.2 Electo-Optics

The data used in this thesis was primarily gathered from the Space Surveillance Telescope (SST), which is an EO system developed by Defence Advanced Research Projects Agency (DARPA). The main advantage of EO systems over radar systems for SSA is their ability to more easily detect objects around 36,000 km often associated with geosynchronous orbits [17]. While radars have the ability to determine range and range rate information which EO systems do not, it requires significant power SSA radars to search for objects above 5,000 km [17]. Passive EO systems collect light reflected to Earth and are not limited by the same power restrictions. With an increasingly crowded geosynchronous orbit, which contains many military satellites that provide critical capabilities to warfighters, protecting them from collision with space debris, meteors and microsatellites has become a top priority [19].

In general, EO systems work by collecting and focusing electromagnetic radiation in the light spectrum reflected by an orbital object into an image. This means that SSA EO systems only work when the target is illuminated by the sun and the telescope is in darkness [17]. This constraint primarily affects the detection aspects of SSA. Most detection algorithms work by finding contrasts in light intensity from the background light levels. This is why daylight detection remains difficult as the contrast between daylight light levels and objects trying to be observed is very small. Most often, observations made by EO systems are only made during the local nighttime.

1.3 The Space Surveillance Telescope

Most Earth-based telescopes are unable to see objects such as micro-satellites and space debris that threaten military satellites. The SST was developed by DARPA beginning in 2002 to overcome these limitations by enabling ground-based, broad-area search, detection and tracking of small objects in deep space for purposes such as space mission assurance and asteroid detection [2]. The US Congress mandated that National Aeronautics

and Space Administration (NASA), with the help of the Department of Defense (DoD), to catalog by the year 2020 at least 90 percent of comets and asteroids larger than 140 meters that are in Earth orbit or come within close proximity of Earth [4]. The SST was designed to scan space to detect and correlate unknown space objects rather than dwell on stellar objects over relatively long periods of time [20]. The SST uses a 3.5 meter aperture which allows for significantly better performance for detecting dim objects in space over other current SSA optics. Additionally, the large aperture allows for the SST to have a wide field of view allowing the SST to provide full sky coverage with frequent revisit times in the hopes of detecting and cataloging Earth orbiting objects and NEAs within its field-of-view. In general, the SST tracks along the sky at the sidereal rate; this means stars appear to be stationary, while objects within the solar system appear to move across the Charge-Coupled Device (CCD) array from frame to frame. As the time between each frame is known and the position can be determined in the CCD array, it is possible to measure the angular position and angular velocity of a detected object. Of note, the data used in this thesis was gathered as the SST was in a test mode which tracked a communications satellite, ANIK-F1, in geostationary orbit. In this case, the stars appeared to move across the sky at the sidereal rate [20].

Many of the current SSA telescopes have difficulty finding and tracking small objects across wide tracks of sky [7]. The SST was designed with these two limitations in mind to look primarily for objects in geosynchronous orbit and to provide a much wider angle (6 square degrees) field-of-view from which to view the wide tracks of the sky. The SST is a 3-mirror Mersenne-Schmidt type telescope with a 3.5 m primary mirror with a short focal ratio of F/1.0 [19]. Additionally, there is a 1.75 m secondary mirror; this secondary mirror acts like a stop making the aperture of SST appear donut shaped with an outer diameter of 3.5 m and in inner diameter of 1.75 m. Figure 1.1 shows the layout of SST's 3 mirrors. The compact layout of the SST ensures a highly agile pointing system.
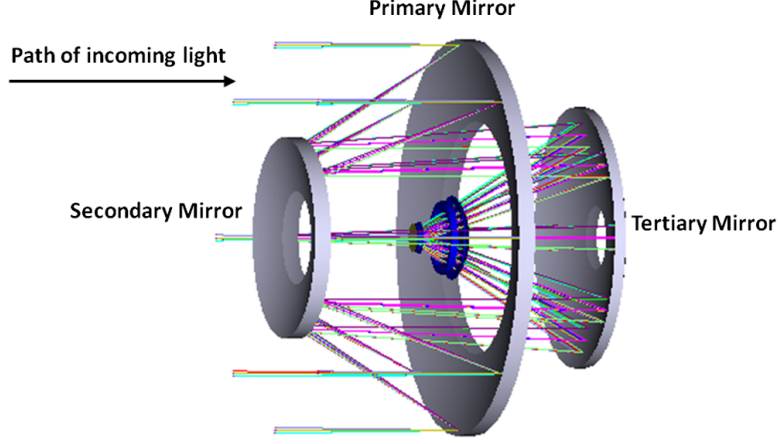
Figure 1.1: Optical layout of the SST [19].

The SST also has a 6 square degree curved CCD focal array to match the telescope's inherently curved focal surface [19]. As the telescope has an extremely short focal ratio, F/1.0, with a relatively large field-of-view, the curved CCD focal array allows for light entering at any angle within the 6 square degrees FOV to be focused properly at the 3.5m focal length of the telescope. The 6 square degree FOV is composed of 3×2 degrees FOV; to capture this FOV, the curved CCD focal array is 12288×8192 pixels [19]. Each pixel is a square $15\mu m$; thus the CCD array is approximately $18.43cm \times 12.29cm$.

Note, the terms pixel, CCD, and photodetector are used interchangeably throughout this thesis and refer to the same thing. Additionally, the terms intensity and irradiance are also used interchangeably throughout this thesis and are considered equivalent for the purposes of this research.

1.4 Detectors

There are two main types of detection algorithms used in this thesis. The first type uses a Binary Hypothesis Test (BHT), which computes a Log-Likelihood Equation (LLE) to form a ratio, often referred to as the Log-Likelihood Ratio (LLR), for each pixel in an image [20]. The LLR is the ratio of an object's likelihood of being in a pixel, denoted as

4

hypothesis H_1, to the likelihood that an object is not in a pixel, denoted as hypothesis H_0. Each hypothesis is given equal likelihood of occurring. If the LLR is above a specified threshold τ, then H_1 is considered to be more likely for a particular pixel, and vice-versa, if the LLR is below τ, then H_0 is considered to be more likely. The probability of detection, P_d, forms an inverse relationship with the probability of false alarm, P_{fa}, in that if the threshold value that determines if H_1 or H_0 is more likely is set too low, then the P_{fa} increases. For this reason, τ is often set higher than 1 in order to reduce the P_{fa} to 6-sigma. Currently, the BHT is the detection method being used on the SST. Section 3.3.1 of this thesis describes the BHT method in greater detail.

The second type of detection algorithm uses a Multi-Hypothesis Test (MHT). The MHT is identical to the BHT method in that the same LLR array of values for a given image are computed; however, the MHT adds an additional step to correlate nine hypotheses with the image data [20]. Each hypothesis is a sampled Point Spread Function (PSF). The use of nine PSFs arise from the fact that an object being observed is not always focused perfectly in the center of a pixel. If an observed point source of light is focused to the middle of two pixels, the intensity profile will be integrated over both pixel areas and the resultant PSF will be appear different from the PSF that is formed if the observed point source is focused and integrated over the area of only one pixel. The nine PSFs are generated from the various combinations of shifting the observed point source up, down, left, and right by half a pixel from the center.

In the MHT, the nine hypotheses are then correlated with the LLR values. The nine generated hypotheses provide a more accurate representation of an object being observed by an EO system and can thus provide a more confident assertion as to whether an object is detected or not. Additionally, the hypothesis with the strongest correlation values can be assumed to represent the actual observed position most accurately. This additional piece of position data is a key piece of information that the MHT provides and can be used to more

accurately determine the angular position of an observed object. Section 3.3.2.2 also refers Multi-Hypothesis Test with Outlier Removal (MHTOR), which contains a slightly different method from MHT in computing the background noise levels that shows some additional improvement over the more traditional MHT. Section 3.3.2 contains more details on the MHT methods. Section 3.2 describes the optical model of the SST and the generation of the nine PSFs in more detail.

1.5 Determining Position

Once an object is detected, then step 2 of the SSA process can occur, which is to determine the angular position and rate of a detected object. The algorithm currently used on the SST to determine the position of the detected object is to centroid the binary map of ones and zeros determined by the BHT. This thesis also examines two other options for determining the position of the detected object. The first alternate option is to use a Center of Intensity (CoI) algorithm. This option uses the binary map of the image determined by the BHT and maps the detection points back to the intensity values of the original image. A centroiding operation is then performed on the intensity values to determine the CoI. This approach has shown some improvement in determining position over centroiding the binary map determined by the BHT. The approach taken with MHT methods is to centroid the Signal to Noise Ratio (SNR) values. Only four of the hypotheses from the MHT were used when scanning through an image as some of the hypotheses are redundant. The corresponding correlation values for the four hypotheses were then input into a matrix that was double the length and width of the original image. The centroiding operation was then performed on this large matrix which has all the correlation values from the four hypotheses. The results from this last method seemed to provide the most accurate position information. Section 3.4 discusses the position algorithms in more detail.

1.6 Measuring Angular Rate

Once the position data has been determined, it is possible to determine the angular rate of a detected object. This is done by measuring the amount of change in an object's position from one frame to the next which is measured in Δ pixels per frame. Using the focal length of the optics and size of each pixel, it is possible to determine what each pixel represents in radians. This ratio is then used to convert Δ pixels per frame into radians per frame. As the time between each frame is known, the angular rate in radians per second can be determined. Section 3.5 describes this process of determining the angular rate of a detected object in more detail.

This thesis primarily uses the angular rate of stars, which have a well known angular rate. Stars appear to orbit the Earth at the sidereal rate. In truth, even the closest stars are over at least 4.4 light years away and their position does not change with respect to Earth's rotation. However, as the Earth rotates once per sidereal day, the stars from a topocentric observation point, appear to orbit the Earth once per sidereal day or 2π radians per 23.9344696 hours. This angular rate is well known to a high degree of precision and accuracy and can then be considered as the truth data by which angular rates calculated as part of this research can be compared against. The least squares method was used to determine a mean and variance for each comparison. Section 3.6 describes the determination of the mean and variance using the least squares method in more detail.

1.7 Errors in Measuring Position

Additionally, EO systems are highly subject to atmospheric conditions that introduce phase aberrations to the propagated wavefront. Specifically, the tilt phase error is the strongest phase error introduced by the atmosphere and has the greatest affect on the observed object's pixel position [15]. The determination of position underlies the ability to determine angular rate and must be considered. Subsection 3.7.1 of this thesis discusses in more detail the effects of the tilt phase error has on the position data gathered by the SST.

1.8 Problem Statement

In a purely deterministic system, the current orbital dynamics of an observed space object are presumed to perfectly known [18]. Based on these orbital dynamics, it is possible to know exactly where an object will be in the future. Under this ideology, measurements of where a space object is are presumed to be perfect. However, atmospheric turbulence and imperfect optics cause errors in the observed position of an object. With atmospheric turbulence being a random phenomenon and the inexact measurement of optical aberrations in optics system, an observation uncertainty when measuring the position of an observed object must be taken into account. Based on the observation uncertainty, an observed position becomes a probability that the object is at a position. This observation uncertainty propagates when trying to predict the future location or track of an object [18]. Therefore, when measuring the position of an object, the precision and accuracy of the measurement are very important parameters for determining the position of an object in the future. In order to improve SSA, it is necessary to reduce the observation uncertainty by improving the accuracy and precision of the measurement.

1.9 Research Objectives and Focus

The primary research objective of this research is to determine which detector from both the point detector BHT and MHT in combination with a centroiding operation are better at determining the position of a detected space object. While research has been done in [20] to show that the MHT is a better detector, no research has been done to determine which detector is better able to provide single frame position information from which angular rate can be calculated when looking at changes in position over multiple frames. The research will focus on determining the angular rate of a star. The primary reason for determining the angular rate of a star is because a star has a very precise and known angular rate providing accurate truth data. As each algorithm will measure an angular rate, it can be compared to the known angular rate to determine which algorithm is most accurate.

8

As each algorithm has some measured error from the actual position, the determination of which algorithm will be done by statistical methods - specifically, the mean and standard deviation will be determined by comparing the measured data against the truth data. Once a particular algorithm is determined to be the most accurate in determining the angular rate of a star, then it can then be used to determine the angular rate of orbiting objects that do not have a known angular rate.

1.10   Assumptions and Limitations

The main limitation for the algorithms developed in this research are that they were developed by windowing the data from the SST to only a single space object per image frame. As the centroid operation used in this research to determine position would be inaccurate if two or more objects were detected in a particular window, it is necessary to window the detected object to a single object. There are clustering operations that can separate multiple objects and thus determine position and angular rates of multiple objects; however, it is outside the scope of this research.

Additionally, as the algorithms for determining position were only verified using the angular movement of stars, which have a known angular rate, it is assumed that the position algorithms as proposed in this research will also function properly in determining the angular rate of an object that has an unknown angular rate.

1.11   Implications

The SST uses the pixel location of three positive detection decisions to build an orbital track of the object which can then be used to predict the future position of the object [20]. The SST currently uses the integer pixel location of points detected using the BHT. This approach does not have sub-pixel location from which to create the track of the detected object; this can lead to large errors in determining the track of the object. The improvements in the detection capability using the MHT have been documented in [20]; however, this

9

detection technique also allows for sub-pixel location data. With a more accurate position algorithm, as proposed in this research, it is possible to reduce the position error of each observation. This in turn, reduces the covariance matrix and thus better estimates of the track can be made.

1.12   Preview

This research aims to demonstrate that the MHT method provides better position information on a detected space object. The position information is used to calculate the angular rate of the detected object; thus, the better position information will lead to determining better tracks of space objects. This research will add to the research that has already been done in [20] to show that the MHT is a superior detector over the currently used BHT on the SST by demonstrating that the MHT can be used to provide better position information as well. Chapter 2 describes the process of how the SST is modeled, the setup of both the BHT and MHT methods to process data from the SST, the description and setup of the position algorithms used in this research, the method for determining angular rate from the position data, and the method for determining which set of algorithms best determined the angular rate from a statistical perspective. Chapter 3 will interpret the results of the analysis and tests run using the position algorithms on the SST data. Chapter 4 discusses the validity of the proposed position and angular rate algorithm based on comparison to the current method being employed on the SST.

II.   Literature Review

2.1   Chapter Overview

This section of the paper provides a survey of some of the relevant literature that has been written concerning the topics of 1) detecting whether an object is present or not in an image and 2) determining the error associated with making dynamics measurements using topocentric measurements of Earth orbiting objects.   Topic 1) is written about by Zingarelli, Pearce, Lambour, Blake, Peterson, and Cain in *Improving the Space Surveillance Telescope's Performance using Multi-hypothesis Testing*. Topic 2) is written by Maruskin, Scheeres, and Alfriend in *Correlation of Optical Observations of Objects in Earth Orbit*.

2.2   Detection Techniques

The Zingarelli, et al. paper describes the purpose of the SST, the BHT detection algorithm, and the MHT detection algorithm and is foundational to much of the research done in this paper. The point of the experiment run in the Zingarelli, et al. paper is to determine which type of algorithm from the BHT or the MHT is best at detecting dim unresolvable objects in space on a single frame basis. In order to run the experiment in the Zingarelli, et al. paper, a satellite, ANIK-F1, in geosynchronous orbit that is gradually going into the eclipse behind the Earth was chosen. This allows the unresolvable satellite to experience a near-continual decrease of solar illumination, thus providing a continuum of irradiance values over which to test the performance of the BHT and the MHT. The results of the experiment run in the Zingarelli, et al. paper show that the MHT method improved the probability of detection P_d by as much as 50 percent over the point detector BHT, which is detection algorithm currently run on the SST.

2.2.1 Relevant Research: Detection Techniques.

The SST uses at a minimum, three sequential detections to determine a track which can be used to predict the future position of an object. The track of an object is based on the position of the object at each detection. Therefore, providing the most accurate position data becomes a critical piece of information in being able to predict the future position of the detected space object. As will be seen in this research, the additional sub-pixel information provided by the MHT will provide a significant advantage in determining the pixel position information over the BHT. This information can then be used to measure the angular position and angular rate of an object which is the primary purpose of this paper. Much of the work in the Zingarelli, et al. paper was primarily aimed at increasing the detection capability of the SST by using the MHT whereas the primary purpose of this research shows that while the MHT increases detection capabilities, it also provides better position information of the detected space object from which better predictions of angular position and angular rate can be made.

2.2.2 The BHT Detector.

Currently, the SST uses a BHT algorithm to detect space objects in a single image [20]. This approach is called the baseline point detector; the other BHT analyzed in the Zingarelli, et al. paper is the matched-filter technique (i.e. correlation detector). Both the point detector test and correlation detector are derived in terms of SNR. The correlation detector was not analyzed in this thesis; while the correlation detector is shown to increase the probability of detection, it does not provide sub-pixel location information. As the primary purpose of this thesis is to measure the angular rate of a detected space object, the correlation detector is not analyzed.

The BHT algorithm works by setting two hypotheses for a given pixel in an image. The null hypothesis H_0 is the hypothesis that a space object is not in a pixel. The alternate hypothesis H_1 is that a space object is in a pixel. If the H_1 hypothesis is more likely for three

successive frames, then an image is considered detected. Additionally, the pixel location of the three positive detection decisions is used to build an orbital track of the object which can then be used to predict the future position of the object. The use of three successive positive detections helps eliminate non-Gaussian noise sources such as cosmic rays and data communication errors arising from the photo-detector, thus reducing the false alarm rate when detecting an object.

The baseline point detector used in the SST can be derived from a Likelihood Ratio Test (LRT) [20]. The BHT is derived in terms of two hypotheses. The hypothesis H_1 is a likelihood that an object is present in the pixel of interest; H_0 is the hypothesis that an object is not present in the pixel of interest. $P(d(x, y) \forall (x, y) \in [1, M_d]|H_i)$ is the joint conditional probability of the data given that $H_i, i \in \{0, 1\}$ is true. Therefore, in the BHT, the LRT becomes a ratio of the hypotheses probabilities. In order to minimize the probability of false alarm, this ratio is not given equal weighting; instead, this ratio must be greater than a threshold value of six in order for the H_1 hypothesis to be considered more likely.

2.2.3   Calculating the Probability of False Alarm for the BHT.

The threshold value inherently sets the probability of false alarm P_{FA} [20]. While a Poisson distribution is a more accurate representation of background noise, a Gaussian distribution can be used to approximate the image noise. In the case of the SST, the threshold $\gamma = 6$ is chosen. Thus, the P_{FA} for the SST is defined as the chance that a pixel that only contains background light (no object) will produce a detector output that exceeds the threshold value of 6 [20]. When an object is not present in a pixel, the ratio produces a unit variance, zero mean Gaussian random variable; therefore, the probability of false alarm per pixel (ignoring non-Gaussian forms of noise) is

$$P_{FA} = P(SNR_{baseline} \geq 6|H_0) = \int_{6}^{\infty} \frac{1}{\sqrt{2\pi}} e^{\frac{-t^2}{2}} dt = 9.87e - 010. \tag{2.1}$$

13

Table 2.1: Alternative Hypothesis Sub-pixel Shifts

Alternative(a)	Horizontal Shift(α_a)	Vertical Shift(β_a)
1	0	0
2	0	$-15\mu m$
3	0	$+15\mu m$
4	$+15\mu m$	0
5	$-15\mu m$	0
6	$+15\mu m$	$-15\mu m$
7	$+15\mu m$	$+15\mu m$
8	$-15\mu m$	$-15\mu m$
9	$-15\mu m$	$+15\mu m$

2.2.4   The MHT Detector.

In the Zingarelli, et al. paper, another matched filter method, the MHT, is proposed for single frame detection. The primary rationale for the introduction of the MHT is because the image of a space object does not always get focused in the center of a pixel. As the shape of a sampled PSF changes depending on where the object is imaged on the CCD array, the correlation with a system PSF with the image data may not correlate strongly. In order to account for the possibility that the space object may be focused off-center of a pixel, a multiple-hypothesis strategy is considered. Each hypothesis is a sampled PSF which is generated by shifting the PSF by plus and minus a half-pixel (which is $15\mu m$ in the SST CCD array) horizontally and vertically as described in Table (2.1); the system PSF is then sampled to create the nine hypotheses. Each hypothesis H_i is then correlated with the data in each pixel. The MHT method selects from nine hypotheses ($H_1 - H_9$) and the null hypothesis H_0 to determine whether the image is in the center, a corner, or a side of

a pixel. The Multi-hypothesis decision to select one hypothesis, H_k, over another one of the other nine hypotheses, H_i, is based on uniform cost and equal priors using conditional probabilities [20].

2.2.5   Calculating the Probability of False Alarm for the MHT.

While the goal of this thesis is not specifically in increasing the detection of space objects, it is important to consider the probability of false alarm of the MHT. Using the Eq. (2.1) and considering each hypothesis to be mutually exclusive from one another and also assuming that the result of each individual sub-MHT to be statistically independent of each other, the P_{FA} is $\approx 4x9.87e - 10 = 3.94e - 9$ [20]. The estimated P_{FA} is higher for the MHT than for the BHT; however, the P_{FA} can be reduced by raising the detection threshold $\gamma_{MHT} = 6.2212$, which yields a $P_{FA} = 9.87e - 10$.

2.2.6   MHT With Outlier Removal.

The Zingarelli, et al. paper also proposes a separate method for computing the standard deviation, σ, of the background noise as listed in Eq. (3.20). This method rejects any noise sample in the window surrounding the pixel to be tested whose values are outside those predicted by Gaussian statistics. This has the effect of eliminating extremely high noise or nearby stars in the calculation of background noise.

2.2.7   Modeling the Point Spread Function for the SST.

In the Zingarelli, et al. paper, a modeled system PSF is used to characterize the SST's impulse response, $h_{optics}(x, y)$. The SST's optics are modeled as linear and shift invariant. The light propagating from a distant point source such as a star or Earth orbiting object is assumed to be temporally incoherent light. The Zingarelli, et al. paper describes a method for generating the system PSF by taking the inverse Fourier transform of the product of the optics, sampling, and atmospheric transfer functions. This method is also utilized in this research.

2.2.8 Summary and Relation to this Research.

The Zingarelli, et al. paper provides the method for implementing the BHT, the MHT, and creating a system PSF. The paper also states that the MHT improved the detection capability of the SST over that of the currently employed point detector test while also providing sub-pixel position information. This research utilizes much of this paper to implement the BHT and MHT. Additionally, this research builds upon the research of this paper by utilizing the sub-pixel position information to determine the angular rate of a space object. By utilizing the better position information of the MHT, this research also shows that the track information that the SST calculates could be improved by utilizing the MHT method.

2.3 Determining the Error Associated with Making Orbital Dynamics Measurements

The Maruskin, et al. article describes a method for determining the orbits of medium to high Earth orbiting objects by determining the intersection of two orbital tracks from two observation points. Due to the large uncertainty associated with measuring and estimating range and range rate values of a detected object, orbital determinations based on these estimates will likewise also have large uncertainties. The Maruskin, et al. article devises an algorithm which does not rely on estimates of range and range rate to perform the initial orbit determination.

From a mathematical perspective, once the angular rates and accelerations are measured for both the right ascension, α, and declination, δ, angles, it is possible to determine the range, ρ, and range rate, $\dot{\rho}$ [11].

2.3.1 Determining the Error in Measuring Angular Position, Rate, and Acceleration and the Observation Uncertainty.

The main value gained from the Maruskin, et al. article is in determining the errors in measuring the angular position, rate, and acceleration of a space object due to observation

uncertainties. Assuming that the angular motion can be modeled kinematically and that the orbit of the detected space object is deterministic in nature, then it is possible to fully determine the orbit of an object [11]. However, from a practical perspective, there is a large uncertainty in measuring the angular position, rate, and acceleration of an orbital object which translates into a large uncertainty in estimating the range and range rate [11]. By using the equations described in the Maruskin, et al. article and further elaborated on in section (3.7.2), it is possible to determine the error associated with measuring angular position, rate, and acceleration using the SST. The calculation of the observation uncertainty parameter used in the calculation of the errors in the angular parameters is elaborated further in section (3.7).

2.3.2 *Maruskin: Summary/How my research is different.*

While the determination of the orbit of a detected object for the purposes of cataloging the object is one of the primary goals of SSA, the method of correlating multiple optical observations as described in the the Maruskin, et al. article is still a new and relatively untried method. Additionally, the method described in the article relies on optical observations that are several minutes apart and from multiple observation points; this is a departure from how the SST operates by taking multiple sequential measurements separated by as little as 0.675 seconds [19]. For these reasons, the orbital determination method described in this article was not utilized in this research. However, the method for calculating the error in the angular parameters is very applicable to the research of this paper.

17

III. Methodology

3.1 Chapter Overview

The key purpose of the research in this thesis is determining the angular rate of a space object, thus determining the most accurate pixel position of an object detected by one of the matched-filter tests is imperative. The SST currently uses the point detector BHT to detect a space object [20]. As the BHT name indicates, the pixels that an object is detected in are indicated with a 1, while the pixels that no object is detected in are indicated with a 0, thus creating a binary map of the sky. If a single space object detected covers more than one pixel, then a centroid operation is used to determine the position of that object; otherwise, the integer value of the detected pixel is the position of the object. This method fails to take into account the intensity or SNR values of a detected object therefore introducing errors into the calculation of position of a detected object. Furthermore, the error in position measurement degrades the accuracy from which the track of the object is determined from the position information of three subsequent positive detections.

Two other methods were analyzed in this research and tested with data from the SST to determine the position of an object; these included performing a CoI algorithm on the BHT and using the SNR values from MHT and centroiding these values. The CoI method maps the detection points from the BHT method back to the original data which contains the intensity values. The intensity values of the pixels immediately adjacent to the detection point were then centroided to determine the CoI and position of the detected object. The other method utilized in this research to determine the position of a detected object is based on the MHT method. The results in the Zingarelli, et al. article show that the MHT method can increase the probability of detection of a space object over the BHT while also providing sub-pixel location data. In the MHT method for determining position, the hypothesis with the highest SNR is selected as the most probable hypothesis. The method

18

of centering the SNR values, referred from this point onward as Center of SNR (CoS), relies on taking the array of SNR values as calculated from each of the hypotheses in the MHT, mapping these to a master array of SNR values from four of the hypotheses, and then performing a centroid operation on the master array to find the position.

The following sections in this chapter explain: 1) the modeling of the system PSF for use in the MHT method, 2) the setup of the BHT and MHT detectors, 3) the methods for determining position of a detected object using the centroid operation on the binary, intensity, and SNR values as determined from the BHT and MHT methods, 4) the method for measuring angular rate, 5) the statistical method to compare each of the angular rate determination methods against each other, and 6) the method for measuring the observation error of the SST and the errors associated in measuring the angular position and rate of a detected object.

3.2   Modeling the PSF of the Space Surveillance Telescope

To create the simulated PSFs, the SST system is modeled in Matlab by using the aberration free (diffraction-limited) incoherent Optical Transfer Function (OTF) of the SST. The phase aberrations, which are departures from an ideal spherical wavefront form due to imperfections in the optics of the SST, were then added to the idealized pupil function to create the generalized pupil function, $\mathscr{P}(x, y)$. The phase aberrations were modeled using Zernike polynomials and were provided by the MIT Lincoln Labs. The resulting intensity PSF is then integrated over the area of a pixel and downsampled to the SST's actual pixel size. This last step creates a pixelated version of the PSF known as the sampled PSF in this research.

The ability to accurately model the PSF of the SST is crucial to being able to run the MHT, which is a matched-filter test relying on the cross-correlation of multiple hypotheses. These hypotheses are alternately sampled PSFs, with the image data from the SST. The underlying assumption for the MHT to be considered valid is that most objects detected by

19

the SST are far enough away and small enough that they can be treated like a point source when observed from the SST. If this assumption is valid, then the data gathered from the SST can be treated as if it is from a point source; therefore, the cross-correlation of the data and the hypotheses is valid. In order to show that detected objects can be treated as a point source, a simple comparison of two similar triangles as in Figure 3.1 is used. In the figure, 3.5m is the focal length of the SST, $30\mu m$ is the effective pixel size, and 36,000km is the approximate distance to geosynchronous orbit. Therefore, the approximate maximum size that a space object at geosynchronous orbit can be and still fit within one pixel is 308.6m. As most space objects that SST is trying to detect are at geosynchronous orbit are smaller than 308.6m, it can be assumed that most objects can be treated simply as a point source. While some asteroids may be much larger than 308m, they are at a much higher altitude than geosynchronous orbit, and thus still remain within the requirements for being treated as a point source. Without this assumption, the cross-correlation of an imaged space object
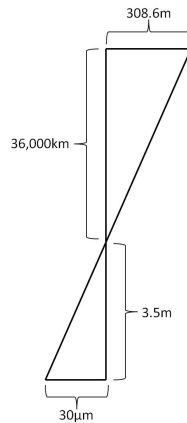
Figure 3.1: Using similar triangles to calculate maximum size of a space object. Note, the figure is not to scale and is drawn for clarification.

and the SST PSF would not be valid.

20

Now that it can be assumed that a detected object can be considered to be a point source, the determination of the system PSF for the SST can be considered. In the Zingarelli, et al. paper, a modeled PSF is used for the characterizing SST's impulse response, $h_{optics}(x, y)$ and is considered the optical PSF. The SST's optics are modeled as linear and shift invariant. The light propagating from a distant point source such as a star or Earth orbiting object is assumed to be temporally incoherent light.

Based on a linear and shift-invariant model for the optical system, the image irradiance, $i(x, y)$, in the CCD array plane with coordinates (x, y), of the continuous image is the convolution of a point source, mathematically expressed as a delta function, $\delta(x, y)$, with a telescope's impulse response, $h_{optics}(x, y)$ [20]. To most accurately model a system's PSF it is necessary to take into account the wavefront errors introduced by the optics aberrations into pupil function, $\mathcal{A}(u, v)$, where u and v represent coordinates in the pupil plane. The wavefront errors are represented mathematically as the first N Zernike polynomials, $\phi_2 - \phi_N$, where N is the maximum number of polynomials needed for a given telescope [20]. The wavefront error is then captured by scaling the Zernike polynomials with a Zernike coefficient, $Z_2 - Z_N$. The total wavefront error, $\mathcal{E}$, is then

$$\mathcal{E}(u, v) = Z_2 \phi_2(u, v) + ... + Z_N \phi_N(u, v). \tag{3.1}$$

The generalized pupil function taking into account telescope aberrations is then represented by

$$\mathcal{P}(u, v) = \mathcal{A}(u, v) e^{[j \cdot \mathcal{E}(u,v)]}. \tag{3.2}$$

To determine the incoherent PSF, the field at the pupil is then propagated using a Fraunhofer propagator to the CCD array, the square of the field is then taken to determine the irradiance [20]. The irradiance is the physically measurable attribute of an optical wavefield [9]. The irradiance pattern is the PSF of the system, which is mathematically represented by

$$h_{optics}(x, y) = \left| \int \int \mathcal{P}(u, v) e^{\frac{j 2\pi (xu + yv)}{\lambda z}} \, du \, dv \right|^2, \tag{3.3}$$

21

where z is the propagation distance and $\bar{\lambda}$ is the mean wavelength of the light wave [9]. The optical transfer function, $\mathcal{H}_{optics}(f_x, f_y)$, is then computed by performing a Fourier transform, $\mathcal{F}$,

$$\mathcal{H}_{optics}(f_x, f_y) = \mathcal{F}\left\{h_{optics}(x, y)\right\}. \tag{3.4}$$

The resulting PSF must then be sampled to account for finite square pixels of the SST, which are $a = 30\mu m$ [20]. Each pixel is represented by a rectangle function. This allows the irradiance pattern, which describes the number of photons arriving at a location (u, v) in the CCD array, to be integrated over the square pixel. The total power $\mathfrak{P}$ incident on the surface area of a photodetector is a function of the responsivity of the detector and the direction of power flow $\vec{k}$ [9]. This is represented mathematically as

$$\mathfrak{P} = \int\int_A p(u, v)\frac{\vec{k} \cdot \hat{n}}{|\vec{k}|}dudv, \tag{3.5}$$

where $\hat{n}$ is a unit vector pointing into the surface of the detector and A is the area of the photodetector. When $\vec{k}$ is nearly normal to the surface, as is the case with the SST, $\mathfrak{P}$ is simply the integral of the power density p over the detector area [9]. The $\mathfrak{P}$ then represents the total amount of photons that arrive over a surface area A over a given amount of time. The operation can be represented by a transfer function, $\mathcal{H}_{pixel}$, which is the Fourier transform, $\mathcal{F}$, of the rectangle function

$$\mathcal{H}_{pixel}(f_x, f_y) = \mathcal{F}\left\{rect(ax, ay)\right\}. \tag{3.6}$$

Additionally, atmospheric turbulence affects the irradiance pattern. As the integration time used on the SST is greater than 25ms, a long-exposure atmospheric transfer function is an acceptable model for atmospheric effects [20]. The atmospheric transfer function is

$$\mathcal{H}_{atm}(f_x, f_y) = exp\left\{-3.44\left(\frac{\bar{\lambda} \cdot z \cdot \upsilon}{r_0}\right)^{5/3}\right\} \tag{3.7}$$

where the radial frequency $\upsilon = (f_x^2 + f_y^2)^{1/2}$ and r_0 is the atmospheric coherence diameter or seeing parameter [8].

22

The overall system impulse response, $h_{model}(x, y)$ centered on a pixel is then the inverse Fourier transform of the product of all the individual transfer functions:

$$h_{model}(x, y) = \mathcal{F}^{-1}\left\{\mathcal{H}_{optics}(f_x, f_y)\mathcal{H}_{pixel}(f_x, f_y)\mathcal{H}_{atm}(f_x, f_y)\right\}. \tag{3.8}$$

A Nyquist sampled PSF would not change the shape of the image irradiance pattern as a function of a sub-pixel shift, Δx [20]. However, as the SST is undersampled and the point source is not always focused in the center of a pixel, the irradiance pattern does change as a function of where the point source is focused. To model these different irradiance patterns, the modeled PSF is down-sampled using the ratio L between the $30\mu m$ pixels of the SST and the Nyquist pixels size from Eq. (3.3). The shifted and down-sampled PSF is

$$h_{samp}(m, \Delta x, n, \Delta y) = \int \int h_{model}(x, y)\delta(Lm - x - L\Delta x, Ln - y - L\Delta y)dxdy, \tag{3.9}$$

and the sampled irradiance is

$$i_{samp}(m, \Delta x, n, \Delta y) = \theta h_{samp}(m, \Delta x, n, \Delta y) + B, \tag{3.10}$$

where B is the background light, and θ is the total number of photons emitted from the object per integration time, and m is the integer value for each pixel location in the CCD array [20]. Using the shifts as described in Table (2.1), the nine different hypotheses used in the MHT in Eq. (3.30) were determined.

In general, the method for generating the system PSF in this research is left unchanged from what is done in [20]. This method for generating the system PSF is based on multiplying the optics, atmospheric, and sampling transfer functions together to form the total system PSF; this is summarized in the following equation:

$$h_{model}(x, y) = \mathcal{F}^{-1}\left\{\mathcal{H}_{optics}(f_x, f_y)\mathcal{H}_{pixel}(f_x, f_y)\mathcal{H}_{atm}(f_x, f_y)\right\}. \tag{3.11}$$

Eqs. (3.4), (3.6), and (3.7) are used to create the total system impulse response $h_{model}(x, y)$; this is the total system or modeled PSF.

The pupil function, $\mathcal{P}(u, v)$, used in Eq. (3.3), is created in MATLAB by creating a 2400×2400 array of ones and zeros to represent the aperture of the SST where the ones represent the aperture opening. The aperture of SST is donut shaped with a 3.5m outer diameter and a 1.75m inner stop; Figure (3.2) depicts the aperture of the SST as represented in MATLAB.
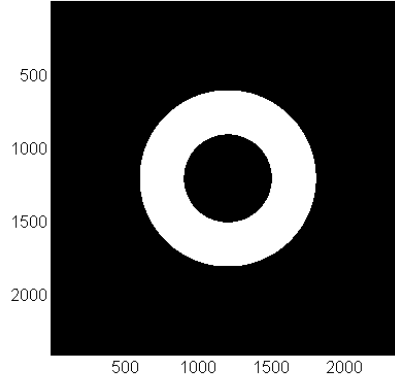
Figure 3.2: The aperture of SST in a 2400×2400 array.

The size of the aperture has a diameter of 1200 samples, which is half of the area the total array. The sampling size is set at 2400×2400 samples to meet Nyquist sampling requirements to avoid aliasing. However, the Fourier transform of a circular aperture, as is the case with the SST, will result in a Bessel function J_1 of the first kind represented by

$$\mathcal{F}\{circ(r)\} = \frac{J_1(2\pi\rho)}{\rho},\tag{3.12}$$

where r represents the radius in the (x, y) plane and ρ is the radius in the two-dimensional spatial frequency plane (u, v) [8]. That being said, the cutoff frequency, f_c, is set by the diameter, D, of the aperture, the focal length, z_f, and the mean wavelength $\bar{\lambda}$ of the light being reflected or emitted in the following relationship [9]:

$$f_c = \frac{D}{\bar{\lambda}z_f}.\tag{3.13}$$

According to Nyquist sampling theorem, the sampling frequency must be at least twice that of the cutoff frequency ($f_s \geq 2f_c$). Therefore, the sampling frequency f_s is:

$$f_s = \frac{2D}{\bar{\lambda}z_f}. \tag{3.14}$$

To satisfy the Nyquist sampling theorem, a 2400×2400 sampling array is selected, which is twice the aperture diameter of 1200 samples. It is also worth noting that by using a $\bar{\lambda} = 500$nm and given that $z_f = D = 3.5m$ for the SST, the sampling period T_s is $0.25\mu m$. For the SST, which has an effective pixel size of $30\mu m$, this means that there are 120 samples per pixel per a given coordinate axis. In general for the SST, the given window that the background noise, B, is calculated from is about a 20×20 pixel window. When considering the 2400×2400 sampling array used for the $\mathcal{P}(u, v)$ is divided by 120 in either coordinate direction, it translates nicely into a 20×20 pixel window. This was purposely set to meet the requirements of Whittaker-Shannon sampling theorem, which implies that the exact recovery of a bandlimited function can be achieved from an appropriately spaced rectangular array of its sampled values [9]. The two-dimensional Fast Fourier transform was then performed in MATLAB on the 2400×2400 array representing the pupil function, $\mathcal{P}(u, v)$, of the SST to determine the diffraction limited OTF, H_{optics}.

Next, in order to create an accurate model of the system PSF, the aberrations or errors in the wavefront due to imperfections in the optics are included. An aberration is any deviation from the ideal, diffraction-limited imaging performance of a lens [1]. Additionally, the Fraunhofer approximations most significantly impact the phase factor of the spherical wave being propagated by approximating them to parabolic wavefronts [9]. Mathematically, lens aberrations can be described by Zernike polynomials, which help express the exit-pupil wavefront of the light being propagated [3]. According to the Woods, et al. paper, the SST's Zernike coefficients for the first twelve Zernike polynomials were estimated using the DONUT algorithm, which generates an estimate of the wavefront aberrations by directly fitting a model of the aberrated image to an observed defocused star

25

Table 3.1: Mean of 36 DONUT Algorithms Run on the SST [19].

Noll index (j)	order (n)	frequency (m)	Classical name	Mean Zernike Coefficient
1	0	0	piston	2.0877
2	1	-1	x-tilt	-5.9517
3	1	1	y-tilt	-5.2999
4	2	-2	defocus	6.8849
5	2	0	y-astigmatism	1.2598
6	2	2	x-astigmatism	-0.2782
7	3	-3	y-coma	0.2755
8	3	-1	x-coma	-0.7279
9	3	1	y-trefoil	0.3548
10	3	3	x-trefoil	-0.4818
11	4	-4	spherical	-0.1567

[19]. The DONUT method was performed on thirty-six defocused stars; the mean of these 36 tests is used as Zernike coefficient. Table (3.1) contains the mean Zernike coefficient for each Zernike polynomial. The equation to model the Zernike polynomials is based on a pyramid where the rows, κ, are the order and the columns, η, are the frequency. The polynomials are defined as

$$
\begin{aligned}
Z_{even_j} &= \sqrt{\kappa + 1}R_\kappa^\eta(r)\sqrt{2}cos(\eta\theta) \quad \eta \neq 0 \\
Z_{odd_j} &= \sqrt{\kappa + 1}R_\kappa^\eta(r)\sqrt{2}sin(\eta\theta) \quad \eta \neq 0 \\
Z_j &= \sqrt{\kappa + 1}R_\kappa^0(r), \qquad\qquad \eta = 0
\end{aligned}
\tag{3.15}
$$

where

$$
R_\kappa^\eta(r) = \sum_{s=0}^{(\kappa-\eta)/2} \frac{(-1)^s(\kappa - s)!}{s!\,[(\kappa + \eta)/2 - s]!\,[(\kappa - \eta)/2 - s]!} r^{\kappa-2s}
\tag{3.16}
$$

Figure (3.3) represents the phase error listed in Eq. (3.1) pictorially. Figure (3.4) shows the non-downsampled PSF from the SST; this is the irradiance pattern of Eq. (3.3), which only takes into account the pupil function and the phase errors of the SST.
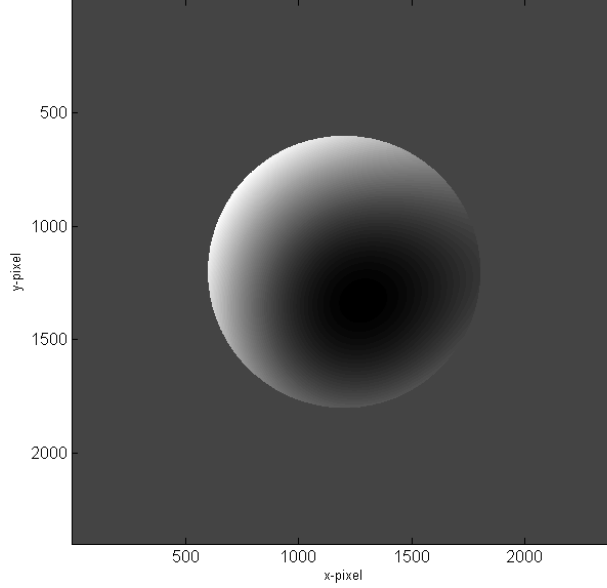
Figure 3.3: The optics phase error ϕ_{error} as modeled by Zernike polynomials.

Next, the atmospheric transfer function, $H_{atm}(f_x, f_y)$, is modeled for the data from the SST using Eq. (3.7). The seeing parameter, r_0, for the data used in this research is determined using a phase retrieval method described in Jeon's research [10]. Table (3.2) lists the r_0 values for the data used in this research.

Depending on where the point source is focused on the CCD array, the system PSF will change. To capture these changes in shape of the system PSF, the convolved PSF must be shifted and then resampled at increments of 120 samples. As one pixel consists of 120 samples, this research shifts the convolved PSF by 60 samples up, down, left and right. This is consistent with the Zingarelli, et al. paper and table (2.1). However, in this research,

27
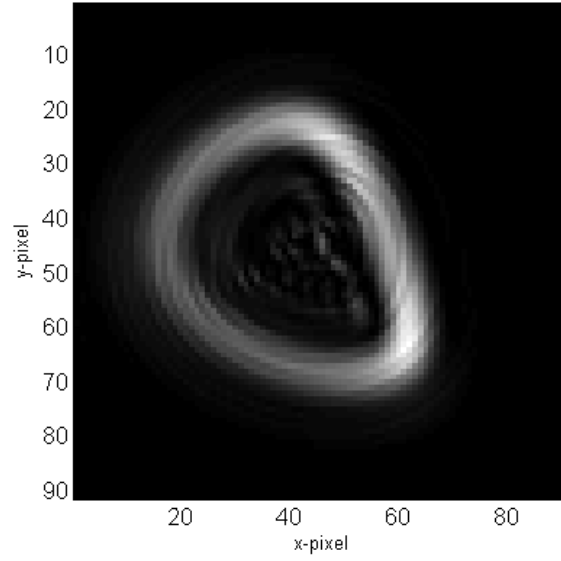
Figure 3.4: Zoomed in image of the SST non-downsampled psf (2400×2400 sample size).

Table 3.2: Seeing Parameters for the Data from the SST

Day	Seeing parameter (cm)
73	5.9
74	6.1
75	5.6
81	3.5
82	4.8
83	6.4

the shifts are done in a different order which is reflected in Table (3.3). These shifted

system PSFs represent the nine hypotheses that are used in the MHT; these hypotheses are

shown in Figure (3.5). Theoretically, an infinite number of hypotheses could be created by

28

Table 3.3: Alternative Hypothesis Sub-pixel Shifts

Hypothesis (H_i)	Horizontal Shift (samples)	Vertical Shift (samples)
1	-60	-60
2	0	-60
3	60	-60
4	-60	0
5	0	0
6	60	0
7	-60	60
8	0	60
9	60	60

dividing the pixel into smaller and smaller shifts; however, in this research, nine hypotheses are chosen in order to keep computation times at a reasonable level.

3.3   Setup of Detection Algorithms in Matlab

The two main detection theories used in this research are the point detector Binary Hypothesis Test (BHT) and the Multi-hypothesis Test (MHT). Both these detection algorithms are considered matched-filter tests and are based on a signal-to-noise-ratio (SNR) that is compared to a threshold value, τ. Essentially, the basic equation for both tests are equivalent. In the BHT, it is a ratio of whether the H_0 hypothesis, which is the likelihood that no object is present in a pixel, as compared to the H_1 hypothesis, which is the likelihood that an object is in a pixel. The MHT takes this one step further by replacing the H_1 hypothesis with multiple hypotheses, each of which are compared to the H_0 hypothesis. Each comparison in the MHT returns a SNR; the highest valued SNR is considered the
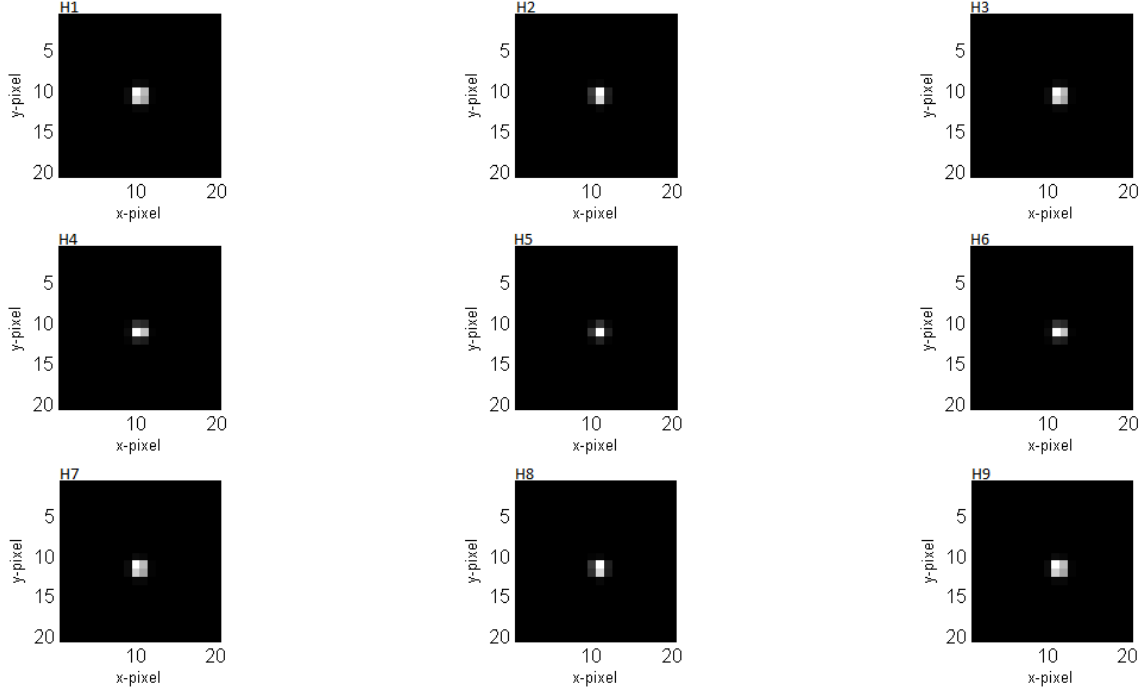
Figure 3.5: Nine hypotheses ($H_1 - H_9$) used in the MHT method

most likely. As each hypothesis in the MHT is created by shifting the focal point on the CCD array, this also has the additional benefit of providing sub-pixel position information for the detected object.

3.3.1 Binary Hypothesis Test.

The baseline point detector used in the SST can be derived from a BHT; it is expressed in a likelihood ratio test (LRT) as follows:

$$\Lambda = \frac{P(d(x, y)\forall (x, y) \in [1, M_d]|H_1)}{P(d(x, y)\forall (x, y) \in [1, M_d]|H_1)} \overset{H_1}{\underset{H_0}{\gtrless}} 1, \tag{3.17}$$

where $d(x, y)$ is the image data, x and y are the pixel coordinates and M_d is the number of pixels in one dimension of a chosen square window in the CCD array plane [20]. The hypothesis H_1 is a likelihood that an object is present in the pixel of interest and H_0 is the hypothesis that an object is not present in the pixel of interest. $P(d(x, y)\forall (x, y) \in [1, M_d]|H_i)$

30

is the joint conditional probability of the data given that $H_i, i \in \{0, 1\}$ is true. Therefore; in the BHT, the LRT becomes a ratio of the hypothesis probabilities.

Using a Gaussian noise distribution to represent the probability $P[d(x, y)|H_i]$ given hypothesis H_1 or H_0, the BHT LRT becomes

$$\Lambda_G = \frac{P[d(x, y)|H_1]}{P[d(x, y)|H_0]} = \frac{\prod\limits_{w=1}^{M_d} \prod\limits_{z=1}^{M_d} \frac{1}{\sqrt{2\pi}\sigma} e^{\{-\frac{1}{2\sigma^2}[d(w,z)-B-\theta h(w,z)]^2\}}}{\prod\limits_{w=1}^{M_d} \prod\limits_{z=1}^{M_d} \frac{1}{\sqrt{2\pi}\sigma} e^{\{-\frac{1}{2\sigma^2}[d(w,z)-B]^2\}}} \begin{matrix} H_1 \\ > \\ < \\ H_0 \end{matrix} 1, \qquad (3.18)$$

where w and z are pixel locations in the window, and the PSF is $h(w, z)$ [20]. The joint conditional probabilities are modeled using a Gaussian noise distribution; though the H_1 joint conditional probability would be more accurately modeled by a Poisson random noise distribution [20]. This is due the noise which limits detection performance is the photon noise of the stars, optical background, and target [14]. As the amount of photons arriving at a target is discrete, yet random, it is most accurately modeled using a Poisson distribution. However, as research in [13] showed that both the Gaussian and Poisson algorithms should have close to the same level of performance if the background master image is flat and small; this allows the master image term to be pulled out of the summation and distributed through the denominator. This results in the same expression for SNR for both the Gaussian and Poisson distributions used for photon statistics [13]. As the SST does not use a master background image, its background noise distribution can be considered flat; therefore, a Gaussian distribution can be used. The value M_d is the total number of pixels in the window of the image [20]. The value B is the background noise level, which is computed as the local sample median of the data. The θ is the space object's irradiance and σ is the standard deviation of the noise and $E[]$ is the statistical expectation operation.

$$B = median[d(w, z)] \; \forall \; (w, z) \; \in [1, M_d] \qquad (3.19)$$

$$\sigma = \sqrt{E[d^2(w, z)] - E[d(w, z)]^2} = \sqrt{\frac{\sum\limits_{w=1}^{M_d} \sum\limits_{z=1}^{M_d} (d^2(w, z) - B)^2}{M_d^2}} \qquad (3.20)$$

31

To simplify Eq. (3.18), the natural logarithm of is taken; this reduces Eq. (3.18) to the following

$$log(\Lambda_G) = \sum_{w=1}^{M_d} \sum_{z=1}^{M_d} \frac{1}{\sqrt{2\pi}\sigma} [-2B \cdot \theta h(w,z) + 2d(w,z) \cdot \theta h(w,z) - (\theta h(w,z))^2] \overset{H_1}{\underset{H_0}{\gtrless}} 0. \quad (3.21)$$

This can further rearranged and simplified to

$$\sum_{w=1}^{M_d} \sum_{z=1}^{M_d} \frac{(d(w,z) - B)h(w,z)}{\sigma} \overset{H_1}{\underset{H_0}{\gtrless}} \frac{\theta}{2} \sum_{w=1}^{M_d} \sum_{z=1}^{M_d} \frac{h^2(w,z)}{\sigma}, \quad (3.22)$$

where the selection of θ will be chosen to achieve the desired threshold γ [20]. To convert Eq. (3.22) into an equation defined in terms of SNR, a new random variable d_2 must be defined. SNR is defined as the ratio of the mean divided by the standard deviation. The new random variable d_2 is the background suppressed data and must have a zero mean in the H_0 case. The random variable d_2 is defined as

$$d_2(w,z) = d(w,z) - B. \quad (3.23)$$

The correlation of the system PSF, $h(w,z)$, with the background suppressed data then becomes

$$\sum_{w=1}^{M_d} \sum_{z=1}^{M_d} d_2(w,z)h(w - c_x, z - c_y) \quad (3.24)$$

where c_x and c_y are the coordinates of the pixel being tested [20]. It can be shown that the H_0 case has a mean μ_2 of zero by

$$\mu_2 = E\left[\sum_{w=1}^{M_d} \sum_{z=1}^{M_d} d_2(w,z)h(w - c_x, z - c_y) \right]$$
$$= \sum_{w=1}^{M_d} \sum_{z=1}^{M_d} E[d_2(w,z)]E[h(w - c_x, z - c_y)] = 0, \quad (3.25)$$

and a variance, σ_2^2, of

$$
\begin{aligned}
\sigma_2^2 &= E\left[\left(\sum_{w=1}^{M_d}\sum_{z=1}^{M_d} d_2(w,z)h(w-c_x,z-c_y)\right)^2\right] \\
&= E\left[\sum_{w=1}^{M_d}\sum_{z=1}^{M_d} d_2(w,z)h(w-c_x,z-c_y)\sum_{w=1}^{M_d}\sum_{z=1}^{M_d} d_2(m,n)h(w-c_x,z-c_y)\right] \\
&= \sum_{w=1}^{M_d}\sum_{z=1}^{M_d}\sum_{m=1}^{M_d}\sum_{n=1}^{M_d} E[d_2(w,z)]E[d_2(m,n)]h(w-c_x,z-c_y)h(m-c_x,n-c_y).
\end{aligned}
\tag{3.26}
$$

Using two cases, Eq. (3.26) can be solved. The first case is when $w \neq m$ and $z \neq n$; the second case involves using the Dirac delta function, $\delta(w-m, z-n)$, and is valid when $w = m$ and $z = n$. Evaluating Eq. (3.26) using these two cases, it reduces to

$$
\sigma_2^2 = \sigma^2 \sum_{w=1}^{M_d}\sum_{z=1}^{M_d} h^2(w,z).
\tag{3.27}
$$

The standard deviation of the normalized data correlated with the total system PSF is simply the square root of Eq. (3.27). Using the standard deviation, it is now possible to express the LRT in terms of SNR [20]

$$
SNR_{corr} = \frac{\sum_{w=1}^{M_d}\sum_{z=1}^{M_d}(d(w,z)-B)h_{corr}(w-c_x,z-c_y)}{\sigma\sqrt{\sum_{w=1}^{M_d}\sum_{z=1}^{M_d} h_{corr}^2(w,z)}} \underset{H_0}{\overset{H_1}{\underset{<}{>}}} \frac{\frac{\theta}{2}\sum_{w=1}^{M_d}\sum_{z=1}^{M_d}\left[(h_{corr}(w,z))^2\right]}{\sigma\sqrt{\sum_{w=1}^{M_d}\sum_{z=1}^{M_d} h_{corr}^2(w,z)}} = \gamma.
\tag{3.28}
$$

The PSF $h_{corr}(w,z)$ is the sampled PSF [20]. In the case of the baseline point detector BHT, $h_{corr}(w,z)$ is one pixel represented as a delta function, $\delta(w-c_x,z-c_y)$; this reduces Eq. (3.28) to

$$
SNR_{baseline} = \frac{\sum_{w=1}^{M_d}\sum_{z=1}^{M_d}(d(w,z)-B)\delta(w-c_x,z-c_y)}{\sigma\sqrt{\sum_{w=1}^{M_d}\sum_{z=1}^{M_d}\delta(w,z)}} = \frac{(d(c_x,c_y)-B)}{\sigma}\underset{H_0}{\overset{H_1}{\underset{<}{>}}}\gamma.
\tag{3.29}
$$

3.3.2 Multi-Hypothesis Test.

There are two forms of the MHT used in this research. Both forms rely on using nine hypotheses, $H_1 - H_9$, that are then correlated with the image data. The only difference

between the two methods is in the calculation of the standard deviation of the background noise. In the basic MHT, the noise is simply the standard deviation, σ, of the background, B. In the MHT plus method, the outliers in the background noise, such as bright stars, are removed; this has the effect of lowering the background noise standard deviation, referred to as ζ in the MHT plus method. Being in the denominator of the MHT equation, this increases the SNR in cases where there are strong noise outliers in the observed image.

3.3.2.1 *Basic Multi-hypothesis Test.*

The SNR equation for the MHT is

$$SNR_a = \frac{\sum\limits_{w=1}^{M_d} \sum\limits_{z=1}^{M_d} (d(w,z) - B) h_{samp}(w - c_x - \alpha_a, z - c_y - \beta_a)}{\sigma \sqrt{\sum\limits_{w=1}^{M_d} \sum\limits_{z=1}^{M_d} h_{samp}^2(w,z)}} \mathop{\gtrless}\limits_{H_0}^{H_a} \gamma_{MHT}, \qquad (3.30)$$

where α_a and β_a represent the half-pixel horizontal and vertical shifts respectively of the sampled PSF. This allows the MHT to provide both detection information as well as sub-pixel position information. The MHT is in contrast to the BHT which only tests whether an object is in a pixel or not. Theoretically, more hypotheses would provide a greater level of sub-pixel location and increase detection performance; however, a finite amount of hypotheses were picked in order to make the test numerically practical. In performing the MHT method, the hypothesis that maximizes the SNR, while at the same time, increasing the probability of detection is chosen. The choice of the hypothesis with the highest SNR also provides sub-pixel position information on the image location [20].

This article describes three detection strategies that could be used on the SST. The first technique, which is currently being employed on the SST, is the baseline point detector [20]. The second detection method that is described is the correlator or matched filter detector. Both of these methods are considered BHTs. The last method that is proposed is the MHT method. Of these various methods, the MHT is the method that is proposed to improve the detection performance of the SST. Results have shown that the probability

34

of detection by using MHT improved by as much as 50 percent over existing detection algorithms.

The two BHT methods and the MHT are based on testing one hypothesis against another in terms of SNR [20]. The first hypothesis is known as H_0 and theorizes that a space object's image is not in a pixel. The alternative hypothesis, H_1, supposes that there is a space object's image in a pixel. The MHT method further divides a pixel into sub-pixel hypotheses, $(H_1 - H_9)$, and compares them to the H_0 hypothesis. The MHT method gives an advantage by mitigating some of the aliasing caused by the undersampled SST observation images. In the MHT method, the hypothesis that maximizes SNR while increasing the probability of detection (P_d) is chosen thereby providing sub-pixel position information while increasing the P_d over both BHT methods [20]. In determining the precise location of a space object, from which angular rate can be determined over subsequent image frames, the sub-pixel location provided by the MHT method provides a significant advantage over the other detection methods.

The MHT is favored over the correlator detector because the shape of the sampled PSF changes depending on where the object is imaged on the observation pixel array [20]; the correlator detector does not take this into account. In the MHT, the sampled PSF changes depending on the location in the pixel array. These various sampled PSFs give rise to the various hypotheses in the MHT detector. The SNR for the MHT is defined as

$$ SNR_a = \frac{\sum_w^{M_d} \sum_z^{M_d} (d(w,z) - B) h_{samp}(w + c_x - \alpha_a, z + c_y - \beta_a)}{\sigma \cdot \sqrt{\sum_w^{M_d} \sum_z^{M_d} h_{samp}^2(w,z)}} \overset{H_a}{\underset{H_0}{\gtrless}} \gamma_{M-ary}. \qquad (3.31) $$

In equation (3.31), α_a and β_a are the horizontal shift and vertical shift respectively that correspond to a sub-pixel location; the nine hypotheses are derived from combinations of $\pm 15 \mu m$ and $0 \mu m$ shifts in α_a and β_a [20]. These hypotheses, h_{samp}, are then correlated with the image data, $d(w,z)$ minus the background noise, B. The square root portion of the denominator in equation (3.31) normalizes the correlation. The σ denotes the noise standard deviation. Each SNR_a corresponds to a hypothesis, H_a; from this, it is deduced

35

that the maximum SNR_a corresponds to the hypothesis that most accurately reflects the sub-pixel location. The maximum SNR_a is considered the true SNR of the detected object.

$$SNR_{M-ary} = max(SNR_a)$$ (3.32)

The γ_{M-ary} denotes the threshold value that the SNR_{M-ary} must be greater than in order for an object to be considered as detected [20]. Mathematically, a low threshold value increases the probability of false alarm, P_{FA}; for this reason, the threshold value is generally increased in order to minimize the P_{FA}. For SST, the threshold value is set to 6.2212 so that the P_{FA} is 9.87e-10.

By using the MHT, it is hoped that both the detection of earth orbital objects will increase as well as provide additional sub-pixel location information by which more accurate angular rates of orbital objects can be made.

3.3.2.2   Multi-hypothesis Test with outlier removal.

The Zingarelli, et al. paper also proposes a separate method for computing the standard deviation, σ, of the background noise as listed in Eq. (3.20). This method rejects any noise sample in the window surrounding the pixel to be tested whose values are outside those predicted by Gaussian statistics [20]. This has the effect of eliminating extremely high noise or nearby stars in the calculation of background noise. In this alternative method, the background noise, B, is still computed as in Eq. (3.19). The squared deviations, D, from the background within the window are computed by

$$D(m) = (d(m) - B)^2,$$ (3.33)

where m is a pixel in the window around the pixel being tested [20]. The mean, M, of the squared deviation D is

$$M = E[D(m)],$$ (3.34)

36

with a standard deviation of S computed as

$$S = \sqrt{E[D^2(m)] - E[D(m)]^2} = \sqrt{\frac{\sum_{m=1}^{M_d} D^2(m)}{M_d^2} - M^2}. \tag{3.35}$$

The new noise standard deviation, ζ, is then computed by excluding any pixel, m, that is outside three standard deviations from the mean; mathematically, this excludes any pixel, m where $D(m) \geq (M + 3 \cdot S)$. The new standard deviation implemented in the MHT has shown to improve detection performance by lowering the normalizing factor, thus increasing the SNR. This is implemented in Eq. (3.30) by replacing σ with ζ [20].

3.4   Setup of Position Algorithms in Matlab

The position algorithms used in this research are based on the results of the BHT and MHT detection algorithms. There were three types on position algorithms used in this research. The first method, referred to as the centroid method, takes the results of the BHT, which are ones and zeros, and centroids these. In most cases, the BHT identifies a single pixel as a detection. In this case, the integer value of the pixel is used as the position of the detected object. This position algorithm is currently the method employed on the SST. The next method used in this research is the Center of Intensity (CoI) algorithm. This method maps the detected points back to the original data, $d(c_x, c_y)$. The intensity values around and including the detected point are then centroided to get a more accurate position. The last method uses the SNR values from the MHT. In this method, four of the hypotheses' SNR values are recorded in a master array. A centroid operation is then performed on the master array to determine the position. This method has calculated the most accurate position information for a detected space object.

3.4.1   Centroid Algorithm.

The detection of an object in the BHT is done by simply noting in an array whether an object is detected (set to a value of 1) or not detected (set to a value of 0) in the detection array, $\mathcal{D}(x, y)$. Occasionally, a detected object is bigger than a single pixel. In this case, a
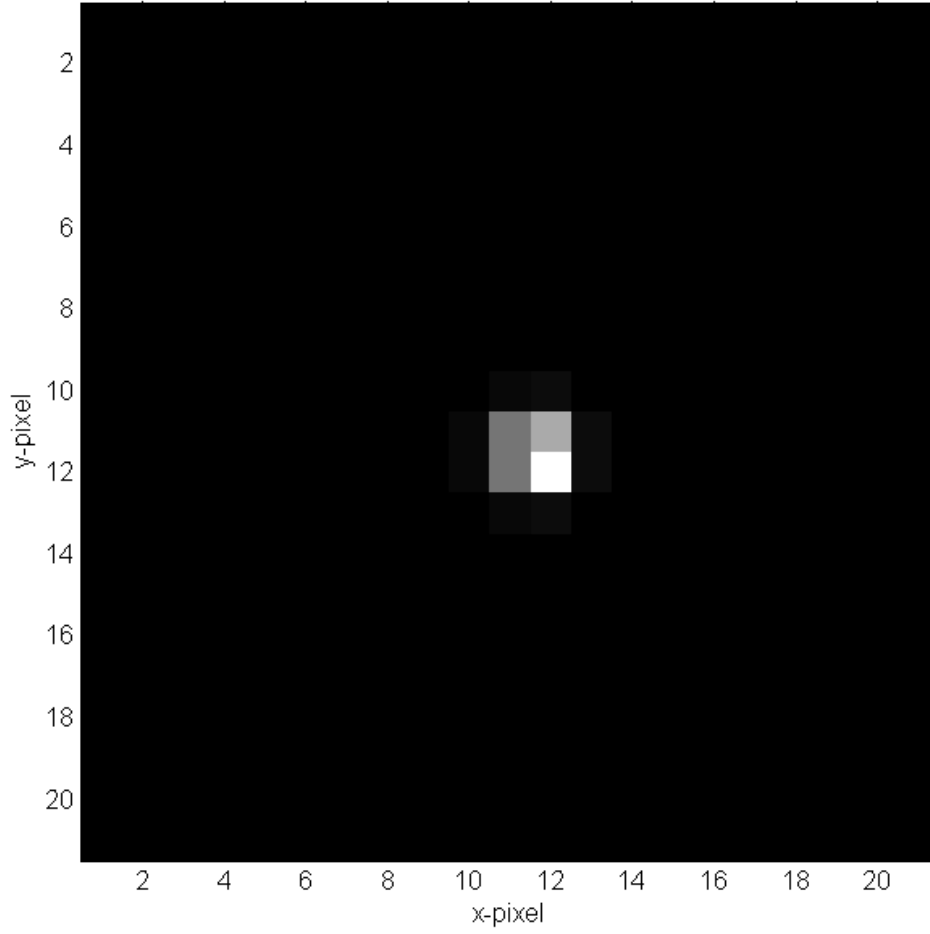
Figure 3.6: Image of star viewed by the SST.

centroid algorithm is used to determine its pixel location. The centroid algorithm for x_{center} (y_{center} is identical) coordinate in the detection array, $\mathcal{D}(x, y)$, of 20 by 20 pixels:

$$x_{center} = \frac{\sum_{x=1}^{20} \sum_{y=1}^{20} \mathcal{D}(x, y) \cdot x}{\sum_{x=1}^{20} \sum_{y=1}^{20} \mathcal{D}(x, y)} \quad (3.36)$$

The detection array is simply an array of ones and zeros marking the detection of objects with the value one. The location in the array of the value corresponds to the pixel location in the actual image frame. Figure (3.6) shows a star observed by the SST. The BHT run on this particular frame of data, shows that four center pixels each met the point detection

38
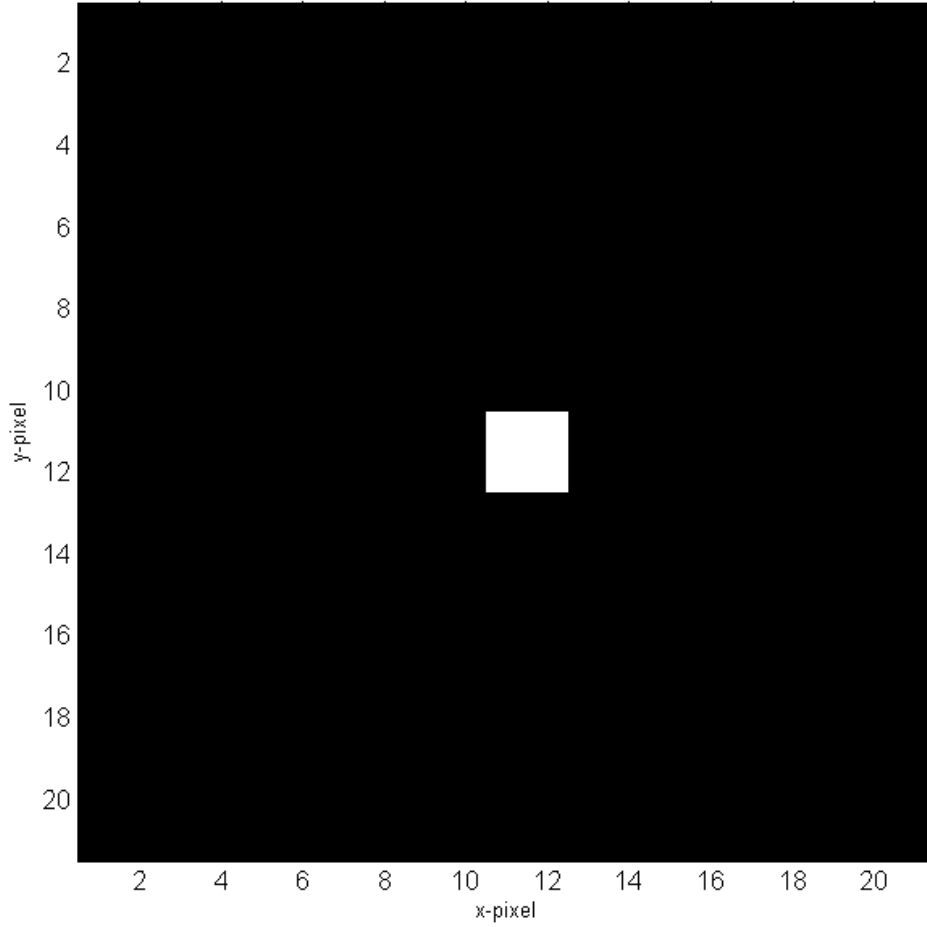
Figure 3.7: Detection array, $\mathcal{D}(x, y)$, from the BHT of star viewed by the SST.

threshold and thus were marked with a value of one; the results of the BHT are shown in Figure (3.7). Using Eq. (3.36) on this figure would yield a position of $(11.5, 11.5)$ as the position of this detected space object. Looking at Figure (3.6), the brightest pixel is $(12, 12)$. It is assumed in this research that the actual position of the object is closer to the $(12, 12)$ pixel; however, as the point detector BHT assigns an equal weighting to detection points and does not take into account the intensity values, that there is an inherent error in the position measurements of the centroid method.

Table 3.4: 4 x 4 array of intensity values, $d_{SST}(x, y)$. In this example, the position of the intensity values would would align with the detection points in Figure (3.7).

Pixel	10	11	12	13
10	0	0	0	0
11	0	30158	43352	0
12	0	30712	65535	0
11	0	0	0	0

3.4.2   Center of Intensity Algorithm.

The center of intensity takes the centroid operation one step further. Instead of performing the centroid operation on the detection array

$$\mathcal{D}(x, y)$$

, the centroid operation is performed on the actual intensity values of the SST data, $d_{SST}(x, y)$. The array of intensity values is determined by multiplying detection array by the original data frame from the SST; this effectively, multiplies by zero anything that does not meet the threshold of the BHT. Figure (3.8) shows an image of $d_{SST}(x, y)$ after it has been multiplied by the detection array $D(x, y)$. The centroid operation is performed using Eq. 3.37. Table (3.4) contains the intensity values of the $d_{SST}(x, y)$ that are used in the centroid example in section 3.4.1.

$$x_{center} = \frac{\sum_{x=1}^{3} \sum_{y=1}^{3} d_{SST}(x, y) \cdot x}{\sum_{x=1}^{3} \sum_{y=1}^{3} d_{SST}(x, y)} \tag{3.37}$$

Using the center of mass equation for the data in table (3.4), the center of intensity is (11.641, 11.567). Based on an observation of the intensity pattern figure (3.8), it should be

40
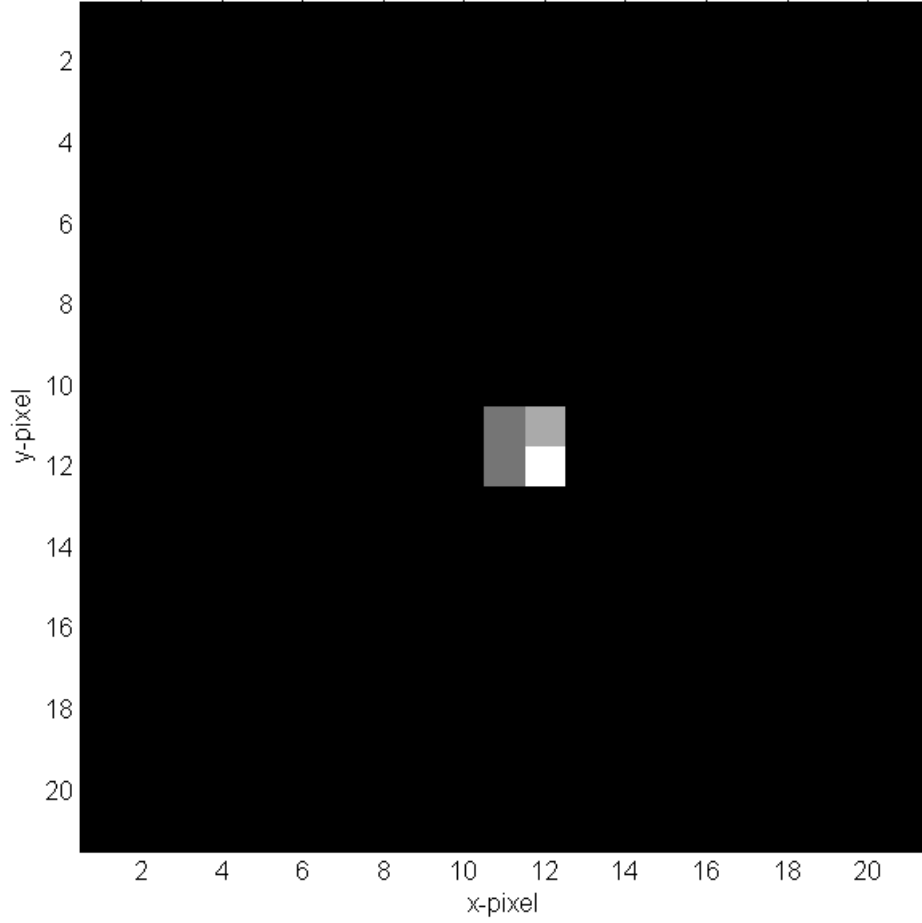
Figure 3.8: The BHT detection points mapped back to intensity values of star viewed by the SST.

more clear that the position of the detected object is weighted and closer to the brightest pixel, which at $(12, 12)$.

3.4.3   Center of SNR Values Algorithm.

The center of SNR (CoS) relies strictly on the results of the MHT method. Each hypothesis is correlated with the underlying SST data. In the correlation operation, the PSF is slid through data and each pixel returns a SNR value. Some of the hypotheses in the MHT have identical intensity patterns, but are shifted in position. For example, in

H5	pixel j		
	15.9937	19.6852	0.0000
pixel k	16.6069	24.1805	0.0000
	0.0000	0.0000	0.0000

H6	pixel j		
	10.9173	21.9504	12.6549
pixel k	10.6927	25.3629	15.4663
	0.0000	0.0000	0.0000

H8	pixel j		
	11.4017	13.3756	0.0000
pixel k	19.8370	26.8860	0.0000
	11.0218	15.9528	0.0000

H9	pixel j		
	7.9665	15.1254	8.6487
pixel k	13.0370	28.8584	17.1181
	7.1383	16.6298	10.4226

SNR master matrix

H5 (j1,k1)	H6 (j1,k1)	H5 (j2,k1)	H6 (j2,k1)	H5 (j3,k1)	H6 (j3,k1)
H8 (j1,k1)	H9 (j1,k1)	H8 (j2,k1)	H9 (j2,k1)	H8 (j3,k1)	H9 (j3,k1)
H5 (j1,k2)	H6 (j1,k2)	H5 (j2,k2)	H6 (j2,k2)	H5 (j3,k2)	H6 (j3,k2)
H8 (j1,k2)	H9 (j1,k2)	H8 (j2,k2)	H9 (j2,k2)	H8 (j3,k2)	H9 (j3,k2)
H5 (j1,k3)	H6 (j1,k3)	H5 (j2,k3)	H6 (j2,k3)	H5 (j3,k3)	H6 (j3,k3)
H8 (j1,k3)	H9 (j1,k3)	H8 (j2,k3)	H9 (j2,k3)	H8 (j3,k3)	H9 (j3,k3)

15.9937	10.9173	19.6852	21.9504	0.0000	12.6549
11.4017	7.9665	13.3756	15.1254	0.0000	8.6487
16.6069	10.6927	24.1805	25.3629	0.0000	15.4663
19.8370	13.0370	26.8860	28.8584	0.0000	17.1181
0.0000	0.0000	0.0000	0.0000	0.0000	0.0000
11.0218	7.1383	15.9528	16.6298	0.0000	10.4226

Figure 3.9: The four hypotheses of the MHT mapped to the SNR master matrix.
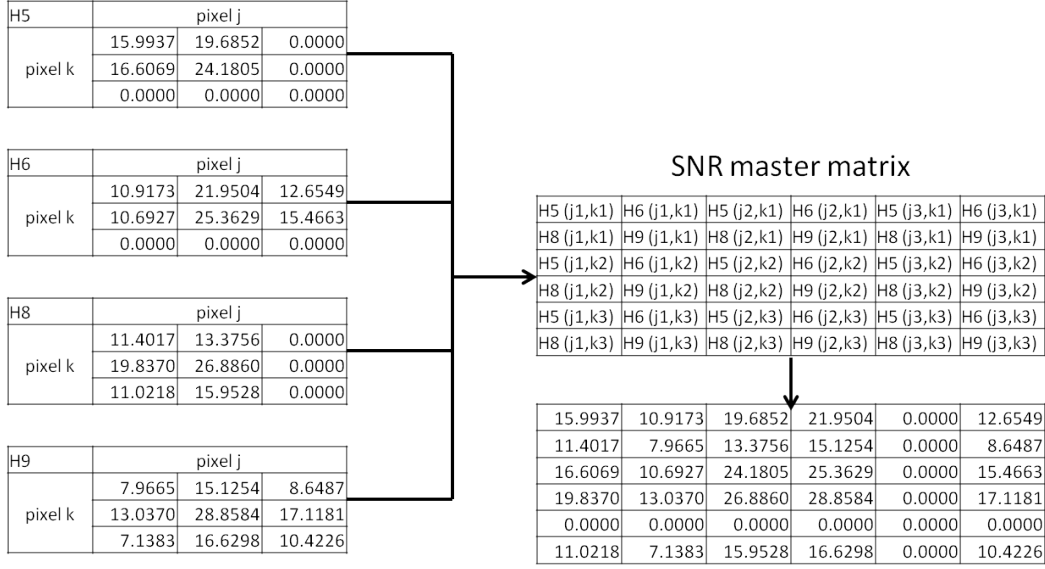
Figure (3.5), $H1, H3, H7$, and $H9$ are identical in their intensity patterns, but are shifted in position. This is true for $H4$ and $H6$, as well as, $H2$ and $H8$. Due to the correlation operation sliding the PSF through the data, these identical PSF intensity patterns will produce identical correlation values with the SST data. For this reason, only $H5$, $H6$, $H8$, and $H9$ are used in this research.

To determine the position using the CoS method, the four hypotheses' SNR values are mapped to a matrix that is double the size of the original data window. Figure (3.9) shows the SNR master matrix values for same example used in the centroid and CoI sections.

The position of the object is found by performing a centroid operation on the SNR master matrix and dividing by two, which accounts for the SNR master matrix being twice the size of the original data matrix. Performing the centroid operation on this example would give a position of $(3.2554, 3.1771)$ on the 6×6 SNR matrix and $(1.6277, 1.5886)$ on the original 3×3 set of observation data. Each of the four hypotheses correspond to a sub-pixel position. The sub-pixel position of the object is then weighted by each of the SNR values
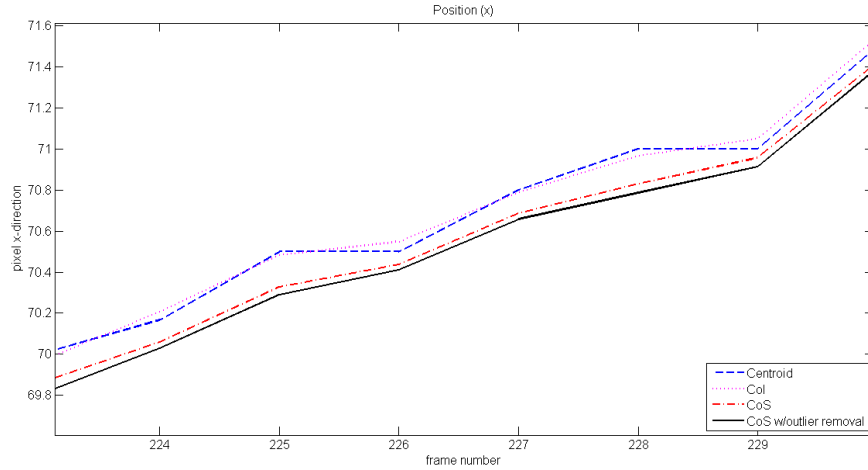
42

Figure 3.10: The difference in position between the MHT position algorithms and the centroid and CoI algorithms.

from each of the hypotheses. In this example, the $H9$ hypothesis has the strongest SNR values. The $H9$ hypothesis corresponds to the bottom, right corner of a pixel. Therefore, in this example, the sub-pixel position is weighted most strongly to the $H9$ sub-pixel position. This approach is performed with both the MHT and MHT plus methods.

It is worth noting that the MHT methods introduce a bias as a result of combining all the SNRs into one master matrix. Figure (3.10) shows an example of this bias in position over several frames of data between the MHT position algorithms and the centroid and CoI position algorithms. As the angular rate is measured by the change in pixel position from frame to frame, the actual position information does not affect the angular rate calculations; however, in this research, a constant is added to the MHT position results to bring the position back in line with the CoI method.

3.5   Measuring Angular Rate from Position Data

Measuring the angular rate from the position data requires at least two sequential frames of data where a space object is detected. Once the position is known in the two

43

frames of data, then it becomes a mathematical operation to measure the change in position over a period of time. As the range of a detected space object is generally unknown, only the angular rate of the detected object can be surmised. Each pixel in the focal array represents an angle in radians of the field-of-view.

3.5.1   Determining Velocity from Position Data.

The next step in this project after detecting an object is to determine an object's velocity in pixels per second. To do this, it involves measuring the change in position (pixel location) between two subsequent frames of the detected object. In this research, the changes is in the x pixel position, represented as Δ_x and the changes in y, denoted as Δ_y, are done separately. Figure (3.11) shows an example of the calculated angular rate in the $x - coordinate$ direction; note that the angular rate in this figure is in radians per frame of data. This is a simple measurement of change between two positions as described by:

$$\Delta_x = x_2 - x_1,$$
$$\Delta_y = y_2 - y_1. \tag{3.38}$$

From the total magnitude of the change in pixel position, Δ_{xy} is also determined using the following equation:

$$\Delta_{xy} = \sqrt{\Delta_x^2 + \Delta_y^2}. \tag{3.39}$$

In this research, only the magnitude Δ_{xy} is considered. While the direction portion of the change vector is important for determining the correct orbit, this research is focused on determining which angular rate algorithm is most accurate. The measurement of the angular rate of a star, which has a well known and precise Δ_{xy}, is used to determine which angular rate algorithm is most accurate.

3.5.2   Transforming Change in Pixel Position into Angular Rate.

In order to determine the angular rate, it is necessary to determine what each pixel represents in terms of radians. This is done by taking the tangent of the size of each pixel,
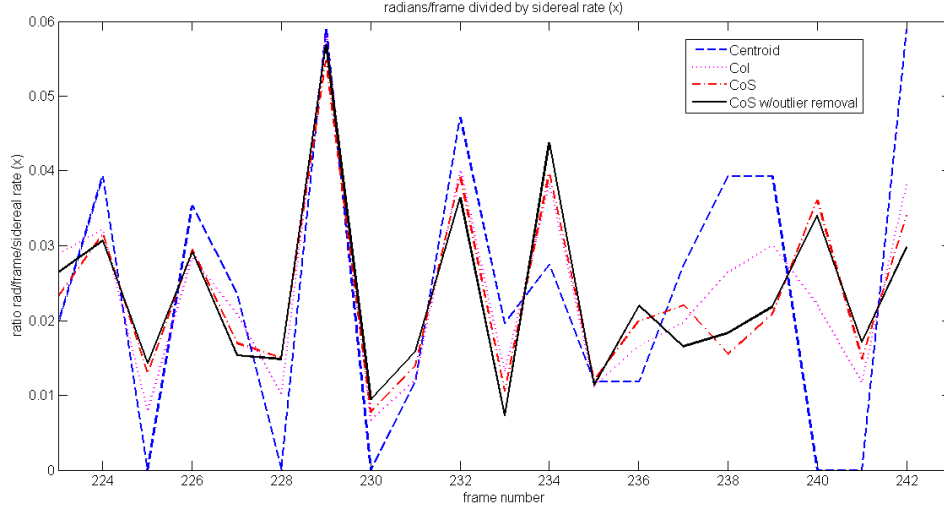
Figure 3.11: Example of calculated angular rate in radians per frame

p_{size}, in the SST divided by the focal length, f, of the SST. The pixel size of the SST is $15\mu m \times 15\mu m$; however, the pixels are binned together in a two by two set effectively creating a $30\mu m \times 30\mu m$ pixel. The focal length of the SST is $3.5m$. Thus the equation for determining what each pixel represents in radians for the SST is:

$$\Delta_\theta = \tan\left(\frac{p_{size}}{f}\right) = \tan\left(\frac{30\mu m}{3.5m}\right) = 8.571\mu rad/pixel. \tag{3.40}$$

The simplest expression for determining the angular rate is Δ_θ divided by the interval of time, t, over which the change occurs. The frames of data used in this research from the SST are taken at 1 second intervals. The angular rate, $\dot{\theta}$, of an objects is then:

$$\dot{\theta} = \frac{\Delta_\theta \cdot \Delta_{xy}}{t} \frac{radians}{second}. \tag{3.41}$$

Figure (3.11) is an example of the total magnitude of the angular rate of a star measured in radians per frame.

3.6 Determination of Statistics

The method for comparing which angular rate algorithm is the most accurate in determining the angular rate is based on statistical analysis. For this research, stars, which have a highly precise and constant angular rate, are used as a way to compare a calculated angular rate with a known angular rate.

Stars appear to make one revolution, 2π radians, of the Earth per sidereal day which is 23.9344699 hours [6]. To calculate the angular rate in radians per second, denoted as $\dot{\theta}_T$, where T represents the true angular rate. The true angular rate of a given star is

$$\dot{\theta}_T = \frac{2\pi}{(23.9344699 hrs \cdot 3600 sec)} = 72.921 \mu rad/sec. \tag{3.42}$$

To simplify the interpretation of the data, the calculated angular rate was divided by the true angular rate of a star. As only stars are used in this research, the ratio of calculated angular rate divided by the true angular rate should be approximately equal to one. Figure (3.12) shows an example plot of this ratio; as can be seen in the plot, the angular rate hovers around 1.

There are two ways to compare the three angular rate algorithms, centroid, CoI, and CoS, used in this research. The first method involves determining the average of the angular rate measurements. Mathematically, this is simply the expected value, $E[]$, of all calculated angular rates, $E[X]$, where X is the data set consisting of the angular rate measurements at each point, $(\dot{\theta}_{N-1}, \dot{\theta}_{N-2}, ..., \dot{\theta}_2, \dot{\theta}_1)$, and N represents the number of sequential frames where a star is detected. The angular rate algorithm with expected value closest to a value of one can then be considered the most accurate method. A concern about using this method is that there can be large variances in the calculated angular rate while still having an expected value close to one. The SST builds its tracks for a detected object from only three detections; therefore, the variance of the angular rate becomes a significant factor.
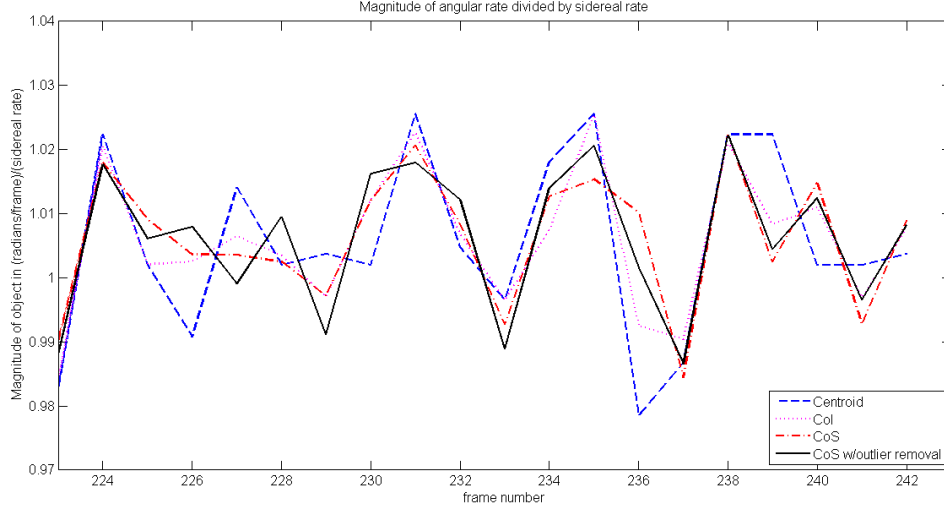
Figure 3.12: Example of calculated total magnitude of angular rate in radians per frame divided by sidereal rate

To calculate the variance of the angular rate, the standard mathematical expression for variance is used; the variance is

$$\sigma^2 = E\left[\left(X - E[X]\right)^2\right]. \tag{3.43}$$

The angular rate algorithm that has the smallest σ^2 can be considered the most consistent algorithm.

The comparison of angular rate algorithms can then be made on two bases. First, the output of the most accurate angular rate algorithm can be made on the comparison with the true angular rate, $\dot{\theta}_T$, by determining the expected value of the observation data set, X. Second, a judgment on the consistency of measurement of the angular rate calculation based on the variance of the observation data set can be measured.

3.7 Error Estimation

The two primary sources of phase errors on a light wave as it propagates from the source in space to the SST are atmospheric turbulence and the optics of the SST [15].

47

These phase errors in the wavefront have an effect on measuring the position of a detected object. As the Zernike coefficients used to model the SST are based on a mean of 36 DONUT algorithms run, it is assumed that these are most accurate method to determine the Zernike coefficients, therefore this section will not discuss this type of phase error in more detail. The tilt phase aberration due to atmospheric turbulence, which causes an object to be shifted in position in the observation plane, is the most significant error associated with atmospheric turbulence; therefore, this section will deal primarily with analyzing the effects due to tilt. The error associated with making measurements of position using an optics system is called the observation uncertainty. The first part of this section will deal with determining the observation uncertainty for the SST based on various tilt phase errors. The second part of this section will deal with how the observation uncertainty affects the measurements of angular position, rate, and acceleration.

3.7.1 *Lower Bound on Position Error Due to Atmospheric Tilt.*

Atmospheric tilt phase error affects the performance of the SST by changing the geometric position of the target on the detector plane. The long exposure tilt is often treated as a Gaussian random variable with a zero mean and unit variance [15]. Figure 3.13 shows an example of the Gaussian shape and blurring effects on a long exposure image. However, at any given instant in time, tilt only causes a translation or shift in the geometric position of the observed object. The observed images at these instants in time are often referred to as short exposure images. Figure 3.14 shows an example of the diffraction limited PSF generated by the SST. Notice that the PSF is slightly off the center point of (600, 600) in the image; it is actually closer to the (609, 600). The short exposure PSF example shows a translation due to atmospheric turbulence, but no blurring due to atmospheric turbulence.

These data used in this project from the SST have an exposure or integration time of 100ms. This integration time has characteristics of both a long and short exposure image. In order to model SST, the 100 ms integration time is divided evenly into 1 ms increments.

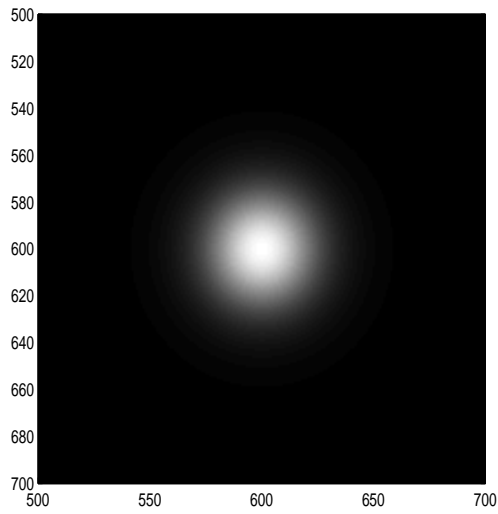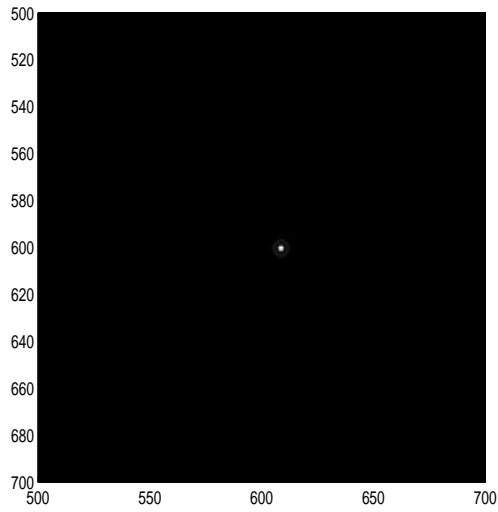Figure 3.13: Long exposure with $r_0 = 15$cm

Figure 3.14: Short exposure with $r_0 = 15$ cm

A phase screen is generated for each 1 ms increment and a corresponding PSF is generated from each phase screen. The 1 ms increment is chosen in order to eliminate the effects of

49

any time averaging of the image due to the atmosphere continually and rapidly changing with time. The general guideline that a short exposure image is somewhere between 0.01 and 0.001 seconds or shorter depending on the wind velocity [8].

Fried's seeing parameter, r_0, is used to generate each phase screen and was considered to stay constant over the 100 ms integration time. Each phase screen that is generated is statistically correlated with the preceding phase screen in order to accurately model the temporal behavior of the atmosphere [15]. The atmospheric phase screen is assumed to evolve in time via Taylor's frozen flow hypothesis [15]. Taylor hypothesized that temporal variations of turbulent eddies at a point are produced by the horizontal transport of atmospheric properties of these turbulent eddies by the mean wind speed flow and not by changes in the turbulent eddies themselves [5]. The time scale associated with temporal variation of the turbulent eddies due to wind is typically on the order of 1 second, whereas the temporal variations of the eddy turnover is much slower, typically on the order of 10 seconds [5]. The effect of the wind on the turbulent eddies is to translate the phase screen a distance in the horizontal and vertical directions equal to the wind velocities, v_x and v_y, multiplied by the time between the sample images Δt [15]. In this research, Δt was 1 ms. The relationship between the phase errors and wind speed at times t_1 and t_2 under Taylor's frozen flow hypothesis is equal to Eq. (3.44) [15] where the atmosphere is considered statistically homogeneous [5].

$$\theta_{atm}(w, s, t_1 + \Delta t) = \theta_{atm}(w + v_x\Delta t, s + v_y\Delta t, t_1) \tag{3.44}$$

The statistical correlation between each phase screen is defined by the phase structure function for Kolmogorov turbulence

$$D_\theta(\tau_x, \tau_y) = 6.88\Big(\frac{\tau_x^2 + \tau_y^2}{r_0^2}\Big)^{5/6} \tag{3.45}$$

50

where $\tau_x = w_2 - w_1$ and $\tau_y = s_2 - s_1$ represent the spatial frequencies in the x and y directions respectively. Equation 3.45 is then used to determine the phase structure function

$$D_\epsilon(\Delta t) = \int_{-\infty}^{+\infty} P_\epsilon(\tau_x, \tau_y)[D_\theta(\tau_x + v_x\Delta t, \tau_y + v_y\Delta t) - D_\theta(\tau_x, \tau_y)]\partial\tau_x\partial\tau_y \qquad (3.46)$$

where P_ϵ is the aperture function [15]. The phase structure function $D_\epsilon(\Delta t)$ is then used to compute the tilt correlation $D_\epsilon(\Delta t)$ through the following relationship:

$$D_\epsilon(\Delta t) = 2R_\epsilon(0) - 2R_\epsilon(\Delta t). \qquad (3.47)$$

$R_\epsilon(0)$ is equal to the variance of the horizontal tilt σ_ϵ^2 and the vertical tilt σ_β^2. Both σ_ϵ^2 and σ_β^2 are considered equal and are related to the aperture diameter D_r and the seeing parameter r_0 through the following equation [15]:

$$\sigma_\epsilon^2 = \sigma_\beta^2 = R_\epsilon(0) = 0.448\left(\frac{D_r}{r_0}\right)^{5/3}. \qquad (3.48)$$

Equation 3.48 is the Zernike-Kolmogorov residual error for the tilt phase errors ϵ and β developed by Noll [12]. $R_\epsilon(\Delta t)$ is the temporal autocorrelation and is the expected value of the product of the tilt at two different times. This is mathematically expressed as: $R_\epsilon(\Delta t) = E[\epsilon(t_1)\epsilon(t_2)]$ [15]. Once $R_\epsilon(\Delta t)$ is known, the conditional probability of the tilt at time $t_1 + \Delta t$ given the tilt at time t_1 is a Gaussian random variable with a mean equal to [15]

$$E[\epsilon_2|\epsilon_1] = \epsilon_1 \frac{R_\epsilon(\Delta t)}{\sigma_\epsilon^2}. \qquad (3.49)$$

The conditional variance is for the Gaussian random variable is

$$E\left[\left(\epsilon_2 - \epsilon_1\frac{R_\epsilon(\Delta t)}{\sigma_\epsilon^2}\right)^2\Big|\epsilon_1\right] = \frac{\sigma_\epsilon^4 - R_\epsilon^2(\Delta t)}{\sigma_\epsilon^2}. \qquad (3.50)$$

Once the conditional mean and variance are known, new phase screens can be generated. The new conditional tilt value ϵ_2 (the same equations apply to β_2) is given by

$$\epsilon_2 = \epsilon_1\frac{R_\epsilon(\Delta t)}{\sigma_\epsilon^2} + \sigma_\epsilon g_2 \qquad (3.51)$$

51

where g_2 is a normally distributed pseudorandom number [15]. The new tilt phase error is

$$\theta_{atm_2}(u, s) = \epsilon_2(u/D_r) + \beta_2(v/D_r). \qquad (3.52)$$

The atmospheric transfer function $H_{atm}(u, v)$ is then equal to $e^{j\theta_{atm_2}(u,v)}$. The total transfer function is $H_{tot}(u, v) = H_{atm}(u, v)H_{optics}(u, v)$ [15]. $H_{optics}(u, v)$ is the optical transfer function of the SST and includes the SST's optical aberrations defined by Zernike polynomials 2 through 12. $H_{tot}(u, v)$ is then used to create a new random conditional PSF for each 1 ms increment.

In this research, only one phase screen per 1 ms increment is used to model the effects of the atmospheric turbulence. Propagation along a slant or vertical path requires an index of refraction structure parameter, $C_n^2(h)$, that changes as a function of altitude (h) [5]. The size of an object and the distance that the light propagates from that object forms an angle θ. If this angle is less than the isoplanatic angle, then the atmospheric turbulence can be modeled with a single phase screen because the angle over which atmospheric turbulence is modeled is essentially unchanged [5]. One of the most popularly used atmospheric turbulence models to express the $C_n^2(h)$ parameter is the Hufnagel-Valley (H-V) model. This is mathematically described in equation 3.53 where h is in meters [m], w is the rms windspeed in m/s and A is a nominal value of $C_n^2(0)$ at the ground in $m^{-2/3}$ [5].

$$C_n^2(h) = 0.00594(w/27)^2(10^{-5}h)^{10}e^{-h/1000} + 2.7 \cdot 10^{-16}e^{-h/1500} + Ae^{-h/100} \qquad (3.53)$$

An often used version of Hufnagel-Valley is determined by setting $w = 21m/s$ and $A = 1.7 \cdot 10^{-14}m^{-2/3}$; this is commonly referred to as H-V$_{5/7}$ [5]. For a wavelength $\lambda = 0.5\mu m$, the 5 in H-V$_{5/7}$ means that a value of 5cm is calculated for the atmospheric coherence diameter and the 7 refers to a 7 μrad isoplanatic angle [5]. Considering H-V$_{5/7}$, about the largest object that can be observed at geosynchronous orbit (36,000 km) and still meet the criteria under H-V$_{5/7}$ for the 7 μrad isoplanatic angle is 252.0m; see Figure 3.15. It can be assumed that most of the objects observed by the SST are smaller than 252.0m

and therefore meet the criteria of being isoplanatic. Therefore, the use of only one phase screen to model the phase error from atmospheric turbulence is valid.
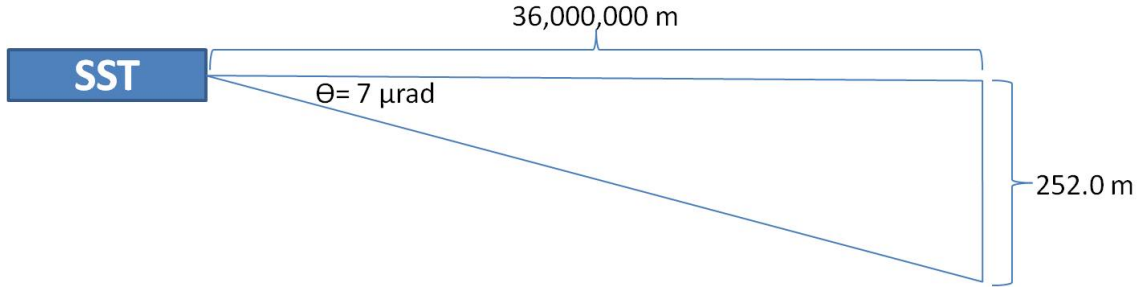

Figure 3.15: Isoplanatic Angle, θ. Note, the figure is not to scale.

The final step to create a representative 100ms exposure image from SST is to average all 100 short exposure 1 ms PSFs together to create a mean PSF. The mean PSF is considered to be an accurate representation of an image generated by the SST over the 100 ms integration time. The mean PSF is then downsampled and integrated using Eq. (3.6) over each pixel to create a sampled PSF. Figure 3.16 shows an example of a simulated 100 ms image by SST.

In order to measure the amount of translation for each mean PSF, the center of intensity algorithm described in Section 3.4.2 is implemented to find the position of the sampled PSF. The translated position is then compared to a "true" PSF where no tilt was introduced and the magnitude of its difference is recorded. To find the magnitude of the difference, G, between the two center of intensity points, a simple vector magnitude equation was used as described in Eq. (3.54).

$$|G| = \sqrt{(y_{center_2} - y_{center_1})^2 + (x_{center_2} - x_{center_1})^2} \tag{3.54}$$

The magnitude of the difference could then be thought of as an the error in observed pixel location from the true pixel location.
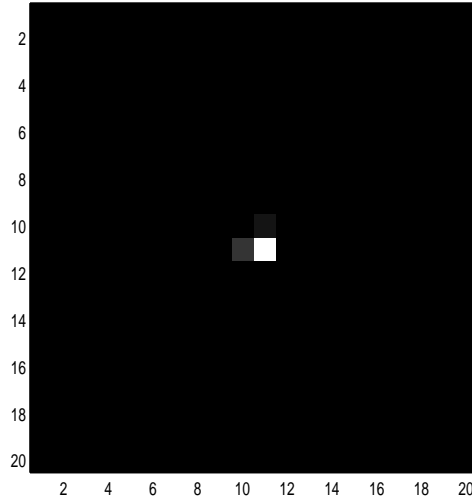
Figure 3.16: Simulated 100ms image as seen by SST

The phase screen generated for each r_0 is generated by a statistical random process. It is possible to find a statistical mean and variance for this random process. To do the statistical analysis, 30 repetitions are run for a particular r_0 and wind velocity and the magnitude of position error is recorded for each repetition. The mean value of the position error is expected to be near 0 for each r_0 value as the tilt phase error is random process that is based on a zero mean Gaussian distribution. The standard deviation of the position error over the 30 repetitions is the key statistical parameter that is trying to be determined in this research. The standard deviation can be thought of as an error in pixel position for a given r_0 and wind velocity for the SST.

In this research, 394 simulations were run without Poisson noise. Another 197 were run with the inclusion of Poisson noise added to the sampled PSF. The numbers of simulations run was restricted to the amount of time available for research. In both simulations, the equation representing the best line fit did not change after approximately 100 simulations. Additionally, The inclusion of Poisson noise represents a more accurate

model as the arrival of photons is a random event; therefore, on average there is an expected number of photons arriving at any given time interval. However, the actual amount arriving at any given moment is best described by the Poisson impulse process [8]. If K is the random variable representing the number of photons arriving at a given time interval and $\lambda(t)$ represents the rate function or mean number of photons arriving for a time interval, then the probability, $P(K; t_1, t_2)$, that K photons fall within the time interval $(t_1 < t \leq t_2)$ is given by [8]

$$P(K; t_1, t_2) = \frac{\left(\int_{t_1}^{t_2} \lambda(t)dt \right)^K exp\left(\int_{t_1}^{t_2} \lambda(t)dt \right)}{K!}. \qquad (3.55)$$

Each simulation performed 30 repetitions for a specific r_0, wind x-direction, and wind y-direction values generated from a Gaussian random number generator in order to provide statistical significance.

The results of these simulations showed an decreasing error in position as r_0 values increased; these results are shown in figure (3.17) and (3.18). In figure (3.17) and (3.18),
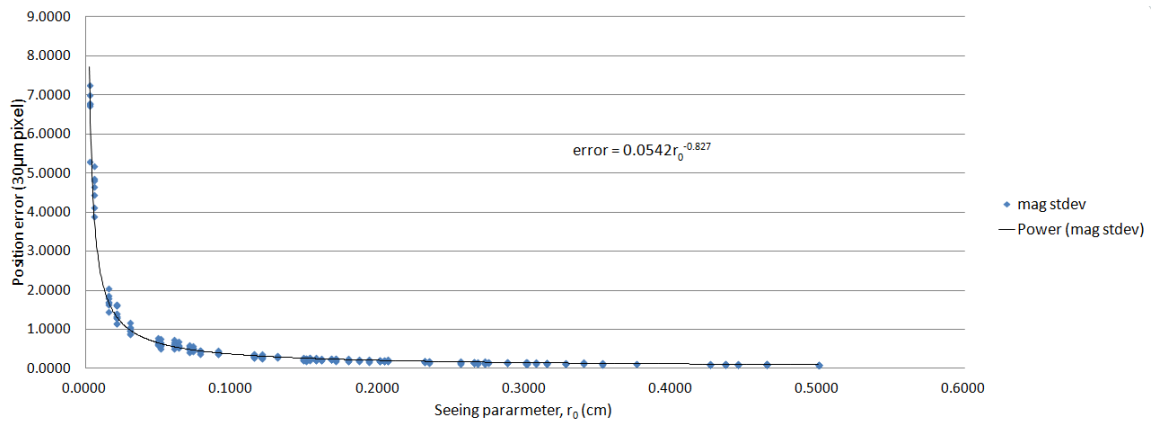

Figure 3.17: Position error $\pm 1 \Phi_{error}$ vs. r_0

the y-axis is $\pm \Phi_{error}$ in units of pixels; the x-axis is the r_0 values in units of centimeters. A
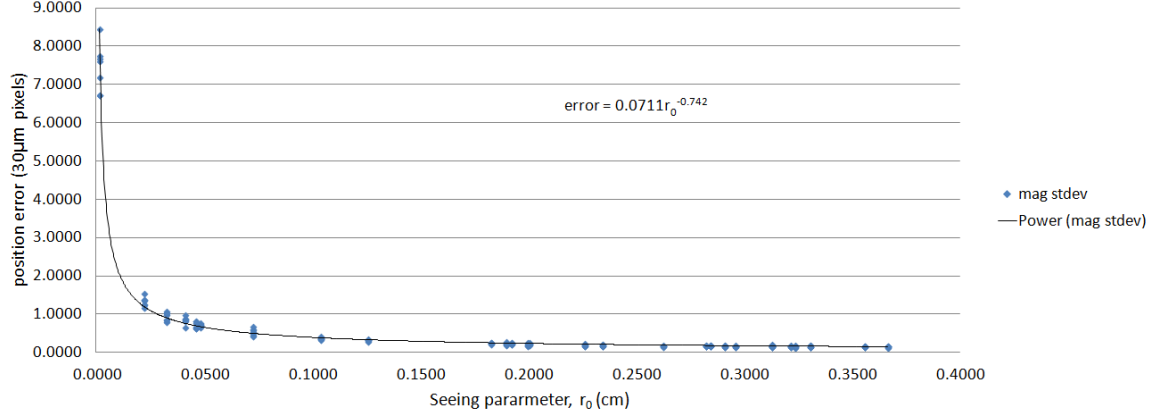
Figure 3.18: Position error $\pm 1\Phi_{error}$ vs. r_0

best line fit in Microsoft Excel was used on the $\pm$ 1 standard deviations line (marked with diamonds in figure 3.17). The best line fit equation is:

$$\pm 1\Phi_{error} = 0.0542 r_0^{-0.827} \tag{3.56}$$

and

$$\pm 1\Phi_{error} = 0.0711 r_0^{-0.742} \tag{3.57}$$

for the model with Poisson noise. It is interesting to note that the inclusion of Poisson noise actually reduced the error due to the Poisson function eliminating small values, thus reducing the size of the sampled PSF. Eqs. (3.56) and (3.57) states that for a particular r_0 value that the position of the object has an error of $\pm 1\Phi_{error}$ in units of pixels. For example, if the SST took an image through a turbulent atmosphere with a r_0 value of 10cm, using the model without Poisson noise, a potential error from its true position in pixel position would be $\pm$ 1.0917 pixels. Assuming the object being observed by SST is in geosynchronous orbit at approximately 36,000km, this would correspond to about 168.44m observed difference from its true location. Note, Eqs. (3.56) and (3.57) are specific for images observed by the SST with an integration time of 100ms.

56

It was also observed from the data that lower wind speeds (near $0m/s$) for a specific r_0 caused higher observed position errors. The opposite is also true that higher wind speeds caused lower observed position errors. However, as r_0 increased, the difference (or variance) between high and low wind speeds decreases. The worst case situation would be a very turbulent atmosphere (low r_0 value) and a low wind speed. This makes sense from a physical perspective as large scale turbulent eddies cause tilt [5]; if the wind is not blowing, the tilt caused by that turbulent eddy will remain in the field of view causing the observed image to be translated.

Eqs. (3.56) and (3.57) can be considered the observation uncertainty and take into account both the imperfections in the optics of a system and the tilt phase error due to atmospheric turbulence. This model allows for the observation uncertainty, referred to as Φ_α in the next subsection, to change as a function of r_0.

3.7.2 *The Total Observation Uncertainty.*

The observation uncertainty affects the ability to accurately determine the position of a detected space object. The observation uncertainty affects the ability to accurately determine the angular position, rate, and acceleration. From a purely deterministic perspective, once the angular rates and accelerations are measured for both the right ascension, α, and declination, δ, angles, it is possible to determine the range, ρ, and range rate, $\dot{\rho}$ [11]. The two astronomical coordinates, α and δ, combine to specify the a point on the celestial sphere in the equatorial coordinate system. Theoretically, once all the variables of Eq. (3.58) are measured from ground based optical sensors or determined from the equations of motion, then all variables of the state equation of the orbiting object are known and it is possible to calculate the orbit of an object. The ability to determine range and range rate is derived from the equations of motion in which the acceleration of either angle is a mathematical function, where the function is represented by f_α and f_δ, of the angular position, angular rate, range and range rate. In Eq. (3.58), the dot and double dot

above the orbital parameter represent the first and second derivatives of the right ascension, α, declination, δ, and range, ρ. From an optical detection perspective, it is very difficult to determine the range and range rate parameters; however, if acceleration can be measured, then through the equations of motion, the range and range rate data can be determined.

$$\ddot{\alpha} = f_\alpha(\alpha, \dot{\alpha}, \delta, \dot{\delta}, \rho, \dot{\rho})$$
$$\ddot{\delta} = f_\delta(\alpha, \dot{\alpha}, \delta, \dot{\delta}, \rho, \dot{\rho})$$

(3.58)

However, from a practical perspective, there is a large uncertainty in measuring the acceleration, $\sigma_{\ddot{\alpha}_o}$, of an orbital object which translates into a large uncertainty in estimating the range and range rate [11]. By using the equations described in the Maruskin, et al. paper, it is possible to determine the error associated with measuring angular position, rate, and acceleration using the SST.

It is important to consider the errors or observation uncertainties in measuring the angular position, rate, and acceleration of a detected space object. Assume that the angular motion can be modeled kinematically as listed in Eq. (3.59) [11].

$$\alpha(t) = \alpha_o + \dot{\alpha}_o(t - t_o) + \frac{1}{2}\ddot{\alpha}_o(t - t_o)^2$$

(3.59)

Provided there are N equally spaced observations (minimum of $N > 3$ observations) of the same object over a span of time T, it is possible to determine the angle at epoch, α_o, the angular rate at epoch, $\dot{\alpha}_o$, and angular acceleration at epoch, $\ddot{\alpha}_o$. Assuming that the N angular measurements are uncorrelated with each other, a least-squares estimation problem is used to minimize the cost function

$$J = \frac{1}{2\Phi_\alpha^2} \sum_{i=1}^{N} [\alpha(t_i) - \alpha_i]^2,$$

(3.60)

where Φ_α is the observation uncertainty, α_i are the actual measurements, and $\alpha(t_i)$ are the predicted measurements; these quantities are used to estimate α_o, $\dot{\alpha}_o$, and $\ddot{\alpha}_o$. Assuming that the measurements are taken at equal times, then $t_i = t_o + (T/2n)i$, where $i =$

$-n, -(n-1), ..., -1, 0, 1, ..., n$, creating a total of $N = 2n+1$ measurements over the total time span T [11]. Due to taking measurements at equal times, the odd terms of the information matrix Λ sum to zero:

$$\Lambda = \frac{(2n+1)}{\Phi_\alpha^2} \begin{bmatrix} 1 & 0 & \frac{n(n+1)}{6}(\frac{T}{2n})^2 \\ 0 & \frac{n(n+1)}{3}(\frac{T}{2n})^2 & 0 \\ \frac{n(n+1)}{6}(\frac{T}{2n})^2 & 0 & \frac{n(n+1)(3n^2+3n-1)}{60}(\frac{T}{2n})^4 \end{bmatrix}. \tag{3.61}$$

The inverse of this matrix is covariance matrix Q which provides the accuracy of the angle quantities measured:

$$Q = \frac{\Phi_\alpha^2}{(2n+1)} \begin{bmatrix} \frac{9}{4} & 0 & -\frac{15}{2}(\frac{2}{T})^2 \\ 0 & 3(\frac{2}{T})^2 & 0 \\ -\frac{15}{2}(\frac{2}{T})^2 & 0 & 45(\frac{2}{T})^4 \end{bmatrix}. \tag{3.62}$$

By taking the square root of the diagonal entries, it is possible to determine the standard deviation, ψ, of the estimated angular motion variables α_o, $\dot{\alpha}_o$, and $\ddot{\alpha}_o$ listed in Eq. (3.59):

$$\psi_{\alpha_o} = \frac{3\Phi_\alpha}{2\sqrt{2n+1}} \tag{3.63}$$

$$\psi_{\dot{\alpha}_o} = \frac{2\sqrt{3}\Phi_\alpha}{T\sqrt{2n+1}} \tag{3.64}$$

$$\psi_{\ddot{\alpha}_o} = \frac{12\sqrt{5}\Phi_\alpha}{T^2\sqrt{2n+1}} \tag{3.65}$$

The purpose of using position algorithms that improve the position accuracy of a detected space object such, as the CoS method, is to reduce the observation uncertainty. This is in turn reduces the errors associated with making measurements of angular position, rate, and acceleration. As the SST determines the track for a detected object based on three subsequent detections, reducing the observation uncertainty as much as possible is important.

IV. Results

The results on this research are based on a statistical analysis of the calculated angular rate of 30 different stars using the SST data. The data is captured by the SST over three days; 10 random stars are used from each day of data. As the purpose of this research is to determine which position algorithm returns the most accurate angular rate, the stars selected are bright; thus, the ability to detect a space object has no impact in determining the position. In this research, on average, 18.9 frames of sequential data is taken for each star in order that a mean with some statistical significance could be determined. Lastly, the window is limited to only one star; this is to avoid issues where multiple objects are detected in a single frame of data, which would manipulate the centroid operations. In full frame data, an unwindowed frame of data may have multiple detected objects. The ability to determine the angular rate for multiple detected objects would involve a clustering algorithm; however, this research is limited to measuring the angular rate of a single space object.

4.1 Assessing the Position and Angular Rate Algorithms

The results of this research show that from a statistical perspective, that all angular rate algorithms, given 18.9 frames of data on average, will calculate a mean angular rate ratio, $E[\mu]$, for the all 30 stars close to the actual angular rate of a star. As is noted in section 3.6, the calculated angular rate is divided by the actual angular rate of a star; thus, a perfectly calculated angular rate divided by the actual angular rate would produce an angular rate ratio of 1.

Looking at table (4.1) and considering only the statistical mean, $E[\mu]$, of the average angular rate, μ, for each star, the centroid method performs the best (1.0056864) given about 19 frames of data followed in order by the CoI method (1.0057782), the CoS_1 method

Table 4.1: Calculated Mean Angular Rate for Each Angular Rate Algorithm

data day	#of frames	μ centroid	μ CoI	μ CoS$_1$	μ CoS$_2$
73	23	1.0049711	1.0054758	1.0056160	1.0052673
73	21	1.0070785	1.0062551	1.0061252	1.0064317
73	13	1.0052292	1.0055392	1.0042487	1.0040030
73	22	1.0059939	1.0059618	1.0057218	1.0060486
73	20	1.0083811	1.0075002	1.0074646	1.0074760
74	20	1.0053867	1.0057544	1.0060864	1.0060435
74	18	1.0068006	1.0070948	1.0072384	1.0071367
74	19	1.0067455	1.0067682	1.0065905	1.0065977
74	17	1.0049657	1.0052306	1.0064570	1.0066316
74	18	1.0049777	1.0057517	1.0057167	1.0058569
74	14	1.0067543	1.0067997	1.0066813	1.0071213
74	19	1.0057002	1.0058825	1.0059335	1.0060599
74	20	1.0066515	1.0056373	1.0049228	1.0052492
74	21	1.0073051	1.0062502	1.0054367	1.0053855
75	18	1.0043525	1.0045270	1.0047913	1.0047076
75	19	1.0055581	1.0055253	1.0053320	1.0052745
75	19	1.0043362	1.0050875	1.0048318	1.0047935
75	18	1.0044765	1.0044657	1.0048413	1.0045600
75	19	1.0055261	1.0060162	1.0062280	1.0061452
75	19	1.0076103	1.0055851	1.0052363	1.0050916
75	17	1.0026446	1.0042524	1.0056341	1.0056372
75	13	1.0034606	1.0050959	1.0059679	1.0060691
75	19	1.0056633	1.0060919	1.0061616	1.0062177
75	19	1.0055581	1.0055253	1.0053320	1.0052745
74	21	1.0051755	1.0050625	1.0051932	1.0051160
73	19	1.0062770	1.0060259	1.0060197	1.0059555
73	19	1.0042889	1.0051152	1.0055301	1.0056028
73	21	1.0052778	1.0053031	1.0053482	1.0051598
73	21	1.0070172	1.0060705	1.0058571	1.0061884
73	21	1.0064290	1.0076935	1.0078084	1.0076327
$E[\mu]$		1.0056864	1.0057782	1.0058118	1.0058245
$\sqrt{E\left[(\mu - E[\mu])^2\right]}$		0.0012631	0.0008212	0.0008086	0.0008684

without noise outlier removal (1.0058118), and lastly by the CoS_2 method with the noise outlier removal (1.0058245). The performance of the centroid translates to an angular rate of 73.33581μrad/sec compared to the performance of the CoS_2, which corresponds to an angular rate of 73.34589μrad/sec. This is only a difference of 0.01008μrad/sec, meaning that all the methods are very close. The statistical mean, $E[\mu]$, is a measurement of the accuracy of the angular rate methods. However, looking at the standard deviation of the accuracy, $\sqrt{E\left[(\mu - E[\mu])^2\right]}$, the centroid method has the largest variability at 0.0012631, while the CoS_1 is the most consistent at 0.0008086. With that said, each angular rate algorithms would fit well within 1 standard deviation of the other methods standard deviation; therefore, the difference in the accuracy of each measurement could be explained by the statistical randomness of the samples chosen in this research. Analyzing the

variance, $E[\sigma^2]$ of the calculated angular rates, which is a measurement of the precision of the angular rate algorithms, the most precise angular rate algorithm is the CoS_1 algorithm with an average variance of $E[\sigma^2] = 0.0001185$. This is approximately 4 times more precise than the centroid algorithm at $E[\sigma^2] = 0.0004462$. Adding one standard deviation to the mean of the centroid method results in an angular rate ratio of 1.02681. This corresponds to an angular rate of 74.8761μrad/sec. Performing this same operation using the CoS_2 returns an angular rate ratio of 1.01670, which corresponds to an angular rate of 74.1392μrad/sec. The difference between the two is 0.7369μrad/sec.

One method to quantify the quality of the measurement is the variance of estimation error [16]. To compare the algorithms from both an accuracy and precision perspective, Eq. (4.1) is used to quantify the total error, e_{total}, where $E[\sigma^2]$ is the variance, $E[\mu]$ is the mean, and T is the true angular rate ratio. In this research, $T = 1$. The total error will have units of error squared.

$$e_{total}^2 = E[\sigma^2] + (E[\mu] - T)^2 \qquad (4.1)$$

Table 4.2: Calculated ± 3 Standard Deviation of the Angular Rate for Each Angular Rate Algorithm

data day	#of frames	3σ centroid	3σ CoI	3σ CoS$_1$	3σ CoS$_2$
73	23	0.0445912	0.0298581	0.0251999	0.0289219
73	21	0.0392077	0.0296648	0.0271911	0.0292341
73	13	0.0963049	0.0446007	0.0315409	0.0354693
73	22	0.0717623	0.0382374	0.0381151	0.0280439
73	20	0.0724458	0.0364097	0.0303710	0.0280032
74	20	0.0428336	0.0334345	0.0314792	0.0336935
74	18	0.0571243	0.0451754	0.0343813	0.0383804
74	19	0.0569313	0.0316126	0.0299362	0.0202356
74	17	0.1246202	0.0865768	0.0360987	0.0269769
74	18	0.0522510	0.0271277	0.0238602	0.0230673
74	14	0.0361371	0.0239891	0.0178208	0.0195015
74	19	0.0501664	0.0336210	0.0227849	0.0178829
74	20	0.0599039	0.0340425	0.0451242	0.0433622
74	21	0.0671119	0.0452155	0.0362285	0.0329722
75	18	0.0577331	0.0441061	0.0359139	0.0433578
75	19	0.0621439	0.0335418	0.0263784	0.0306161
75	19	0.0526860	0.0375872	0.0382641	0.0367432
75	18	0.0635416	0.0325461	0.0318498	0.0320464
75	19	0.0432926	0.0265838	0.0234228	0.0280347
75	19	0.0484179	0.0317165	0.0362577	0.0360900
75	17	0.1195076	0.0669008	0.0248923	0.0267181
75	13	0.0637285	0.0488859	0.0378567	0.0362041
75	19	0.0692308	0.0441056	0.0389342	0.0328561
75	19	0.0621439	0.0335418	0.0263784	0.0306161
74	21	0.0726213	0.0455256	0.0386212	0.0383896
73	19	0.0625248	0.0342114	0.0345918	0.0339022
73	19	0.0636214	0.0404866	0.0366572	0.0408823
73	21	0.0461279	0.0334492	0.0317194	0.0337131
73	21	0.0508438	0.0377533	0.0303708	0.0322880
73	21	0.0914496	0.0603033	0.0574650	0.0608769
$E[3\sigma]$		0.0633669	0.0396937	0.0326569	0.0326360
$E[\sigma^2]$		0.0004462	0.0001751	0.0001185	0.0001183
e^2_{total}		0.0004785	0.0002085	0.0001523	0.0001523
e_{total}		0.0218743	0.0144379	0.0123399	0.0123398

This method for describing which angular rate algorithm is the most accurate and precise from an equal weighting. This is method for quantifying which angular rate algorithm is best is based on the e_{total}, which assigns equal weighting to the mean, $E[\mu]$, differenced from the true angular rate, T, as well as the error due to the variance, $E[\sigma^2]$, of the calculated angular rate. As this method judges the accuracy and precision from an equal footing, the total error will tell which error source between accuracy and precision has more significance in the overall calculated angular rate. Note that the data in this research are based on the ratio of calculated angular rate compared to the actual angular rate; a perfectly calculated angular rate would yield to an angular rate ratio of 1. Additionally, the total error is computed in percentage squared. Therefore, the total error in these results is a percentage squared from 1.

Based on this, the CoS_1 and CoS_2 algorithms both have a total error of 0.01234. This is slightly better than the CoI algorithm which has a total error of 0.01444. The centroid method scores a 0.02187, which is approximately 1.77 times worse than the CoS methods. Given equal weighting of the variance and mean, the precision, $E[\sigma^2]$, is a more significant factor in calculating the angular rate of a detected space object.

Looking at the total error for the centroid algorithm in terms of angular rate, an e_{total} of 0.02187 would correspond to an error of 1.595μrad/sec. Looking at the total error for the CoS methods in terms of angular rate, which both have an e_{total} of 0.01234, they would correspond to an 0.899μrad/sec in error.

V. Discussion

The results of this research show that both the Center of SNR (CoS) algorithms, which are based on the multi-hypothesis test (MHT) detection algorithms with and without noise outlier removal performed the best in terms of precision and total error when measuring the angular rate of an object. The centroid method is the most accurate; however, its slightly better performance in accuracy is well within one standard deviation of the data. This means that this slightly better performance in measuring the mean angular rate could be explained by variances in the data; therefore, a definitive conclusion about it being more accurate angular rate algorithm cannot be made in this research.

5.1 Relevance of Results

The relevance of these results are that the binary hypothesis and centroid method currently employed on the SST for detecting space objects and determining their position and angular rate information could be improved upon by implementing the MHT detection algorithm and one of the CoS algorithm for determining position and angular rate described in this research. Looking at the total error as described in section (4.1), both CoS algorithms had a total error of 0.01234, while the method currently employed on the SST has a total error of 0.02187. This means that in terms of total error, that the CoS algorithms are approximately 1.77 times better than the currently employed centroid method. The total error in terms of angular rate for the centroid method is 1.595μrad/sec. In comparison, the CoS algorithms have a total error of 0.899μrad/sec. As the SST uses around 3 to 5 sequential observations to determine a track for a detected object, having the most precise and accurate angular rate measurement is critical.

5.2 Future Work

The purpose of this research is in categorizing which angular rate algorithm is accurate and precise. The next step in this research would be to use the angular rate measurements from a detected space object to determine its track and orbital parameters. Additionally, if this research is to be implemented on the SST, the code will need to be streamlined in order that it runs near real-time. This requires understanding the full SST system in order that the MHT detection and CoS angular rate algorithms can be implemented into the current operational system. Finally, more work is required in being able to implement this code with a full SST data frame which can contain multiple objects each moving at a unique angular rate.

5.3 Conclusion

Both CoS methods performed in this research are better at determining the position and angular rate of a detected object than the currently employed centroid method on the SST. This research demonstrated that improvements can be made by using the MHT methods. The implications are that the observation uncertainty will go down, thereby improving the estimated angular position and rate. This in-turn improves the ability to determine the track of a detected space object and improve the ability to perform SSA. Additional research will need to be conducted to quantify by how much tracks of detected space objects are improved by when using the MHT algorithms in conjunction with the CoS algorithms.

Appendix: MATLAB code

A.1 Main MATLAB code

```
%Anthony Sligar

%SST detection


clear; close all; clc;


%Day          seeing (cm)

%73            5.9

%74            6.1

%75            5.6

%81            3.5

%82            4.8

%83            6.4


Bx=2.028436184860734e+03;    %x_correct=x_window+view_x1+B

By=3.075334518833674e+03;    %y


%%%%%%%%%%%%%%%%%%%%%%%%%%%%%%%%%%%%%%%%%%%%%%%%%%%%%%%%%%%%%%%%%%%%%%%%%%

load data_cube073_3d;        %data used

rdata=data_cube073_3d;

load hypo59;                 %loads hypotheses with 5.9 cm seeing parameter


%star1

frame1=552;                  %first frame to view
```

```
frame2=575;                      %last frame to view

view_x1=60;                      %coordinate of 1st x value in viewing range

view_x2=80;                      %coordinate of last x value in viewing range

view_y1=1;                       %coordinate of 1st y value in viewing range

view_y2=200;                     %coordinate of last y value in viewing range




%%%%%%%%%%%%%%%%%%%%%%%%%%%%%%%%%%%%%%%%%%%%%%%%%%%%%%%%%%%%%%%%%%%%%%%%%%

%sets size of psf to the size of the window

if (view_x2-view_x1)>=20

    psf=padarray(hypo,[view_y2-view_y1-19 view_x2-view_x1-19],0,'pre');

    z=psf(:,:,5);

    [num indx]=max(z(:));

    [Yshift Xshift] = ind2sub(size(z),indx); %uses index value to find location of

    psf=circshift(psf,[1-Yshift,1-Xshift]);

else psf=padarray(hypo,[view_y2-view_y1-19 0],0,'pre');

    psf=psf(:,1:(view_x2-view_x1+1),:);

    z=psf(:,:,5);

    [num indx]=max(z(:));

    [Yshift Xshift] = ind2sub(size(z),indx); %uses index value to find location of

    psf=circshift(psf,[1-Yshift,1-Xshift]);

end




%%%%%%%%%%%%%%%%%%%%%%%%%%%%%%%%%%%%%%%%%%%%%%%%%%%%%%%%%%%%%%%%%%%%%%%%%%
```

```
%detection tests and position array
for ii=frame1:frame2
    Dsst=rdata(view_y1:view_y2,view_x1:view_x2,ii);   %load SST frame
    [xcent(ii) ycent(ii) H0]=centroid(Dsst);          %centroid function call
    [xCOI(ii) yCOI(ii) H1]=COI(Dsst);                 %CoI function call
    [xMHT(ii) yMHT(ii) H3]=MHT3(Dsst, psf);           %CoS1 function call
    [xSNR(ii) ySNR(ii) H4]=MHT4(Dsst, psf);           %CoS2 function call
end


%%%%%%%%%%%%%%%%%%%%%%%%%%%%%%%%%%%%%%%%%%%%%%%%%%%%%%%%%%%%%%%%%%%%%%%
%position information
Xloc1=xcent+view_x1+Bx;           %centroid method
Yloc1=ycent+view_y1+By;           %centroid method


XlocCOI=xCOI+view_x1+Bx;          %CoI method
YlocCOI=yCOI+view_y1+By;          %CoI method


XlocSNR=xSNR+view_x1+Bx;          %CoS2 method
YlocSNR=ySNR+view_y1+By;          %CoS2 method


XlocMHT=xMHT+view_x1+Bx;          %CoS1 method
YlocMHT=yMHT+view_y1+By;          %CoS1 method


%%%%%%%%%%%%%%%%%%%%%%%%%%%%%%%%%%%%%%%%%%%%%%%%%%%%%%%%%%%%%%%%%%%%%%%%%
%converts pixels to radians in field of view
radperpix=tan((30/3.49)*10^-6);     %SST rad/pixel
```

```matlab
sid_radsec=(2*pi/(23.9344699*3600)); %sidereal rate (rad/sec)


%%%%%%%%%%%%%%%%%%%%%%%%%%%%%%%%%%%%%%%%%%%%%%%%%%%%%%%%%%%%%%%%%%


for kk=frame1:frame2-1
    xslope(kk)=(Xloc1(kk+1)-Xloc1(kk))*radperpix;        %centroid method
    yslope(kk)=(Yloc1(kk+1)-Yloc1(kk))*radperpix;        %centroid method


    xslopeCOI(kk)=(XlocCOI(kk+1)-XlocCOI(kk))*radperpix; %CoI method
    yslopeCOI(kk)=(YlocCOI(kk+1)-YlocCOI(kk))*radperpix; %CoI method


    xslopeSNR(kk)=(XlocSNR(kk+1)-XlocSNR(kk))*radperpix; %CoS2 method
    yslopeSNR(kk)=(YlocSNR(kk+1)-YlocSNR(kk))*radperpix; %CoS2 method


    xslopeMHT(kk)=(XlocMHT(kk+1)-XlocMHT(kk))*radperpix; %CoS1 method
    yslopeMHT(kk)=(YlocMHT(kk+1)-YlocMHT(kk))*radperpix; %CoS1 method


end


%%%%%%%%%%%%%%%%%%%%%%%%%%%%%%%%%%%%%%%%%%%%%%%%%%%%%%%%%%%%%%%%%%%%


%centroid method
xslope1=xslope./sid_radsec; %ratio between object's angular rate to sidereal rate
yslope1=yslope./sid_radsec;
combinedmag=(sqrt((xslope.^2)+(yslope.^2)))./sid_radsec;
avgCen=ones(1,length(combinedmag))*mean(combinedmag(combinedmag~=0));
```

```
pstdCen=avgCen+(ones(1,length(combinedmag))*3*std(combinedmag(combinedmag~=0)));

nstdCen=avgCen-(ones(1,length(combinedmag))*3*std(combinedmag(combinedmag~=0)));


%CoI method

xslopeCOI1=xslopeCOI./sid_radsec; %ratio between object's angular rate to sidereal

yslopeCOI1=yslopeCOI./sid_radsec;

combinedmagCOI=(sqrt((xslopeCOI.^2)+(yslopeCOI.^2)))./sid_radsec;

avgCOI=ones(1,length(combinedmag))*mean(combinedmagCOI(combinedmagCOI~=0));

pstdCOI=avgCOI+(ones(1,length(combinedmag))*3*std(combinedmagCOI(combinedmagCOI~=0))

nstdCOI=avgCOI-(ones(1,length(combinedmag))*3*std(combinedmagCOI(combinedmagCOI~=0))


%CoS2 method

xslopeSNR1=xslopeSNR./sid_radsec; %ratio between object's angular rate to sidereal

yslopeSNR1=yslopeSNR./sid_radsec;

combinedmagSNR=(sqrt((xslopeSNR.^2)+(yslopeSNR.^2)))./sid_radsec;

avgSNR=ones(1,length(combinedmag))*mean(combinedmagSNR(combinedmagSNR~=0));

pstdSNR=avgSNR+(ones(1,length(combinedmag))*3*std(combinedmagSNR(combinedmagSNR~=0))

nstdSNR=avgSNR-(ones(1,length(combinedmag))*3*std(combinedmagSNR(combinedmagSNR~=0))


%CoS1 method

xslopeMHT11=xslopeMHT./sid_radsec; %ratio between object's angular rate to sidereal

yslopeMHT11=yslopeMHT./sid_radsec;

combinedmagMHT=(sqrt((xslopeMHT.^2)+(yslopeMHT.^2)))./sid_radsec;

avgMHT=ones(1,length(combinedmag))*mean(combinedmagMHT(combinedmagMHT~=0));

pstdMHT=avgMHT+(ones(1,length(combinedmag))*3*std(combinedmagMHT(combinedmagMHT~=0))

nstdMHT=avgMHT-(ones(1,length(combinedmag))*3*std(combinedmagMHT(combinedmagMHT~=0))
```

```
%%%%%%%%%%%%%%%%%%%%%%%%%%%%%%%%%%%%%%%%%%%%%%%%%%%%%%%%%%%%%%%%%%%%%%%%%%%%%%

%plotting

figure(1)

subplot(3,2,1)

set(gca, 'FontSize', 12);

plot(Xloc1,'color', 'b','linestyle','--');hold on;plot(XlocCOI,'color','m','linesty

xlim([ frame1 frame2 ])

xlabel('frame number');

ylabel('pixel x-direction');

title('Position (x)')

legend('Centroid','CoI','CoS','CoS w/outlier removal','location','southeast');


subplot(3,2,2)

set(gca, 'FontSize', 12);

plot(Yloc1,'color', 'b','linestyle','--');hold on;plot(YlocCOI,'color','m','linesty

xlim([ frame1 frame2 ])

xlabel('frame number');

ylabel('pixel y-direction');

title('Position (y)')

legend('Centroid','Center of Intensity','MHT','MHT w/outlier removal','location','s


subplot(3,2,3)

set(gca, 'FontSize', 12);

plot(xslope,'color', 'b','linestyle','--');hold on;plot(xslopeCOI,'color','m','line

xlim([ frame1 frame2 ])
```

```matlab
xlabel('frame number');

ylabel('rate (radians/frame) (x)');

title('Angular rate radians/frame (x)')

legend('Centroid','CoI','CoS','CoS w/outlier removal','location','southeast');


subplot(3,2,4)

set(gca, 'FontSize', 12);

plot(yslope,'color', 'b','linestyle','--');hold on;plot(yslopeCOI,'color','m','line

xlim([ frame1 frame2 ])

xlabel('frame number');

ylabel('rate (radians/frame) (y)');

title('Angular rate radians/frame (y)')

legend('Centroid','CoI','CoS','CoS w/outlier removal','location','southeast');


subplot(3,2,5)

set(gca, 'FontSize', 12);

plot(xslope1,'color', 'b','linestyle','--');hold on;plot(xslopeCOI1,'color','m','li

xlim([ frame1 frame2 ])

xlabel('frame number');

ylabel('ratio rad/frame/sidereal rate (x)');

title('radians/frame divided by sidereal rate (x)')

legend('Centroid','CoI','CoS','CoS w/outlier removal','location','southeast');


subplot(3,2,6)

set(gca, 'FontSize', 12);

plot(yslope1,'color', 'b','linestyle','--');hold on;plot(yslopeCOI1,'color','m','li
```

```
xlim([ frame1 frame2 ])

xlabel('frame number');

ylabel('ratio rad/frame/sidereal rate (y)');

title('radians/frame divided by sidereal rate (y)')

legend('Centroid','CoI','CoS','CoS w/outlier removal','location','southeast');


figure(2)

set(gca, 'FontSize', 12);

plot(combinedmag,'color', 'b','linestyle','--');hold on;plot(combinedmagCOI,'color'

xlim([ frame1 frame2 ])

xlabel('frame number');

ylabel('Magnitude of object in (radians/frame)/(sidereal rate)');

title('Magnitude of angular rate divided by sidereal rate')

legend('Centroid','CoI','CoS','CoS w/outlier removal','location','southeast');


figure(3)

set(gca, 'FontSize', 12);

plot(avgCen,'b','linestyle','--');hold on;plot(avgCOI,'m','linestyle',':');hold on;

plot(pstdCen,'b','linestyle','--');hold on;plot(nstdCen,'b','linestyle','--');hold

plot(pstdCOI,'m','linestyle',':');hold on;plot(nstdCOI,'m','linestyle',':');hold on

plot(pstdMHT,'r','linestyle','-.');hold on;plot(nstdMHT,'r','linestyle','-.');hold

plot(pstdSNR,'k');hold on;plot(nstdSNR,'k');hold on;

xlim([ frame1 frame2 ])

xlabel('frame number');

ylabel('Magnitude of object in radians/frame');

title('Magnitude of angular rate divided by sidereal rate using mean and stdev');
```

```matlab
legend('Centroid','CoI','CoS','CoS w/outlier removal','location','southeast');
```

```matlab
%%%%%%%%%%%%%%%%%%%%%%%%%%%%%%%%%%%%%%%%%%%%%%%%%%%%%%%%%%%%%%%%%%%%%%%
```

```matlab
format long;
ZZ=[max(avgCen) max(avgCOI) max(avgMHT) max(avgSNR) max(pstdCen) max(pstdCOI) max(p
```

```matlab
%%%%%%%%%%%%%%%%%%%%%%%%%%%%%%%%%%%%%%%%%%%%%%%%%%%%%%%%%%%%%%%%%%%%%%%
```

A.2   MATLAB code functions: Centroid

```matlab
function [xpos ypos H1] = centroid(Dsst);
```

```matlab
tau=6; %threshold value
%%%%%%%%%%%%%%%%%%%%%%%%%%%%%%%%%%%%%%%%%%%%%%%%%%%%%%%%%%%%%%%%%%%%%%%%%%%%
%point detection test
    Bh=median(Dsst(:)); %this is the noise determined from Dsst
    sigma=sqrt(mean(mean((Dsst-Bh).^2))); %takes the value of all the pixels
    LRT=((Dsst-Bh)/sigma); %LRT is likelihood ratio test

    [m,n]=size(Dsst); %m is size in y direction, n is size in x direction
%%%%%%%%%%%%%%%%%%%%%%%%%%%%%%%%%%%%%%%%%%%%%%%%%%%%%%%%%%%%%%%%%%%%%%%%%%%%
%create matrix of detection points
    for m=1:m
    for n=1:n

    if LRT(m,n)>tau
        H1(m,n)=1; %sets detection parameter H1 to 1 if there is an object
```

```matlab
        else H1(m,n)=0;

        end


    end
end


%%%%%%%%%%%%%%%%%%%%%%%%%%%%%%%%%%%%%%%%%%%%%%%%%%%%%%%%%%%%%%%%%%%%%%%%
%centroid operation
    xsum=sum(H1);

    ysum=sum(H1');

    H1sum=sum(sum(H1));


    for k=1:n %centroid operation; finds x position
        xprod(k)=xsum(k)*k;

    end


    for l=1:m %centroid operation; finds y position
        yprod(l)=ysum(l)*l;

    end
%%%%%%%%%%%%%%%%%%%%%%%%%%%%%%%%%%%%%%%%%%%%%%%%%%%%%%%%%%%%%%%%%%%%%%%%
%returns position coordinates of values
    xpos=sum(xprod)/H1sum; %x position of object

    ypos=sum(yprod)/H1sum; %y position of object


end
```

A.3 MATLAB code functions: CoI

```
function [xpos ypos H1i] = COI(Dsst);


tau=6; %threshold value
%%%%%%%%%%%%%%%%%%%%%%%%%%%%%%%%%%%%%%%%%%%%%%%%%%%%%%%%%%%%%%%%%%%%%%%%%%%%%%%%%
%point detection test
    Bh=median(Dsst(:)); %this is the noise determined from Dsst
    sigma=sqrt(mean(mean((Dsst-Bh).^2))); %takes the value of all the pixels
    LRT=((Dsst-Bh)/sigma); %LRT is likelihood ratio test


    [m,n]=size(Dsst); %m is size in y direction, n is size in x direction
%%%%%%%%%%%%%%%%%%%%%%%%%%%%%%%%%%%%%%%%%%%%%%%%%%%%%%%%%%%%%%%%%%%%%%%%%%%%%%%%%
%create matrix of detection points
    for m=1:m
    for n=1:n


    if LRT(m,n)>tau
        H1(m,n)=1; %sets detection parameter H1 to 1 if there is an object
    else H1(m,n)=0;
    end


    end
    end


%%%%%%%%%%%%%%%%%%%%%%%%%%%%%%%%%%%%%%%%%%%%%%%%%%%%%%%%%%%%%%%%%%%%%%%%%%%%%%%%%
%centroid operation
```

```
    H1i=Dsst.*H1;  %sets values in H1 equal to 1 back to intensity values in Dsst


%%%%%%%%%%%%%%%%%%%%%%%%%%%%%%%%%%%%%%%%%%%%%%%%%%%%%%%%%%%%%%%%%%%%%%%%
%Center of Intensity - COI method 1


    xsum=sum(H1i);

    ysum=sum(H1i');

    H1sum=sum(sum(H1i));


    for k=1:n

        xprod(k)=xsum(k)*k;

    end


    for l=1:m

        yprod(l)=ysum(l)*l;

    end


%%%%%%%%%%%%%%%%%%%%%%%%%%%%%%%%%%%%%%%%%%%%%%%%%%%%%%%%%%%%%%%%%%%%%%%%
%returns position coordinates of values

    xpos=sum(xprod)/H1sum; %x position of object

    ypos=sum(yprod)/H1sum; %y position of object


end
```

A.4   MATLAB code functions: MHT3

```
function [xpos ypos MHT_SNR1] = MHT3(Dsst, psf);
```

```
tau=6.2212; %threshold value


%%%%%%%%%%%%%%%%%%%%%%%%%%%%%%%%%%%%%%%%%%%%%%%%%%%%%%%%%%%%%%%%%%%%

%LRT detection test

    Bh=median(Dsst(:)); %this is the noise determined from Dsst

    sigma=sqrt(mean(mean((Dsst-Bh).^2))); %takes the value of all the pixels

    LRT=((Dsst-Bh)/sigma); %LRT is likelihood ratio test


%%%%%%%%%%%%%%%%%%%%%%%%%%%%%%%%%%%%%%%%%%%%%%%%%%%%%%%%%%%%%%%%%%%%%%

%MHT

    for kk=1:9;


        SNR(:,:,kk)=(ifft2(fft2(LRT).*fft2(psf(:,:,kk))))/sqrt(sum(sum(psf(:,:,kk).^


    end


%%%%%%%%%%%%%%%%%%%%%%%%%%%%%%%%%%%%%%%%%%%%%%%%%%%%%%%%%%%%%%%%%%%%

%filter (set to 0) anything that is less than tau

    [m,n,o]=size(SNR);

    for c=1:o;

    for a=1:m;

    for b=1:n;


        if SNR(a,b,c)>tau

        SNR(a,b,c)=SNR(a,b,c); %sets detection parameter H1 to 1 if there is an obj

        else SNR(a,b,c)=0;
```

```
        end


    end

    end

    end


%%%%%%%%%%%%%%%%%%%%%%%%%%%%%%%%%%%%%%%%%%%%%%%%%%%%%%%%%%%%%%%%%%%%

%create MHT_SNR combined matrix

MHT_SNR=zeros(m*2,n*2);

MHT_SNR(2:2:m*2,2:2:n*2)=SNR(:,:,5);

MHT_SNR(2:2:m*2,3:2:n*2+1)=SNR(:,:,6);

MHT_SNR(3:2:m*2+1,2:2:n*2)=SNR(:,:,8);

MHT_SNR(3:2:m*2+1,3:2:n*2+1)=SNR(:,:,9);

MHT_SNR=padarray(MHT_SNR,[10 10],0,'both');


%%%%%%%%%%%%%%%%%%%%%%%%%%%%%%%%%%%%%%%%%%%%%%%%%%%%%%%%%%%%%%%%%%%%

%filter out all but the brightest star

[m,n]=size(MHT_SNR);

MHT_SNR1=zeros(m,n);

if max(max(MHT_SNR))==0;

    xpos=-1;

    ypos=-1;

else


    [num indx]=max(MHT_SNR(:));

    [Ymax Xmax] = ind2sub(size(MHT_SNR),indx);
```

```matlab
    MHT_SNR1(Ymax-5:Ymax+5,Xmax-5:Xmax+5)=MHT_SNR(Ymax-5:Ymax+5,Xmax-5:Xmax+5);


    %%%%%%%%%%%%%%%%%%%%%%%%%%%%%%%%%%%%%%%%%%%%%%%%%%%%%%%%%%%%%%%%%%%%

    %centroid operation

    xsum=sum(MHT_SNR1);

    ysum=sum(MHT_SNR1');

    H2sum=sum(sum(MHT_SNR1));


    [y,x]=size(MHT_SNR1);


    for k=1:x

        xprod(k)=xsum(k)*k;

    end


    for l=1:y

        yprod(l)=ysum(l)*l;

    end


    %%%%%%%%%%%%%%%%%%%%%%%%%%%%%%%%%%%%%%%%%%%%%%%%%%%%%%%%%%%%%%%%%%%%

    %return position values

    xpos=sum(xprod)/(2*H2sum)-5.5623;

    ypos=sum(yprod)/(2*H2sum)-5.7067;


end
```

A.5   MATLAB code functions: MHT4

```matlab
function [xpos ypos MHT_SNR1] = MHT4(Dsst, psf);
```

```
tau=6.2212; %threshold value


%%%%%%%%%%%%%%%%%%%%%%%%%%%%%%%%%%%%%%%%%%%%%%%%%%%%%%%%%%%%%%%%%%%%%%%%%%%
%LRT detection test
    Bh=median(Dsst(:)); %this is the noise determined from Dsst
    sigma=sqrt(mean(mean((Dsst-Bh).^2))); %takes the value of all the pixels
    binmap=((Dsst-Bh)<tau*sigma); %creates a binary map where 1 is equal to anything
    sigma2=sqrt(sum(sum((binmap.*(Dsst-Bh)).^2))/sum(sum(binmap))); %creates a new
    LRT=((Dsst-Bh)/sigma2); %LRT is likelihood ratio test


%%%%%%%%%%%%%%%%%%%%%%%%%%%%%%%%%%%%%%%%%%%%%%%%%%%%%%%%%%%%%%%%%%%%%%%%%%%
%MHT
    for kk=1:9;


        SNR(:,:,kk)=(ifft2(fft2(LRT).*fft2(psf(:,:,kk))))/sqrt(sum(sum(psf(:,:,kk).^


    end


%%%%%%%%%%%%%%%%%%%%%%%%%%%%%%%%%%%%%%%%%%%%%%%%%%%%%%%%%%%%%%%%%%%%%%%%%%%
%filter (set to 0) anything that is less than tau
    [m,n,o]=size(SNR);
    for c=1:o;
    for a=1:m;
    for b=1:n;
```

82

```matlab
        if SNR(a,b,c)>tau

        SNR(a,b,c)=SNR(a,b,c); %sets detection parameter H1 to 1 if there is an obj

        else SNR(a,b,c)=0;

        end

    end

    end

    end


%%%%%%%%%%%%%%%%%%%%%%%%%%%%%%%%%%%%%%%%%%%%%%%%%%%%%%%%%%%%%%%%%%%%%%%%%

%create MHT_SNR combined matrix

MHT_SNR=zeros(m*2,n*2);

MHT_SNR(2:2:m*2,2:2:n*2)=SNR(:,:,5);

MHT_SNR(2:2:m*2,3:2:n*2+1)=SNR(:,:,6);

MHT_SNR(3:2:m*2+1,2:2:n*2)=SNR(:,:,8);

MHT_SNR(3:2:m*2+1,3:2:n*2+1)=SNR(:,:,9);

MHT_SNR=padarray(MHT_SNR,[10 10],0,'both');


%%%%%%%%%%%%%%%%%%%%%%%%%%%%%%%%%%%%%%%%%%%%%%%%%%%%%%%%%%%%%%%%%%%%%%%%%

%filter out all but the brightest star

[m,n]=size(MHT_SNR);

MHT_SNR1=zeros(m,n);

if max(max(MHT_SNR))==0;

    xpos=-1;

    ypos=-1;

else
```

```matlab
[num indx]=max(MHT_SNR(:));

[Ymax Xmax] = ind2sub(size(MHT_SNR),indx);

MHT_SNR1(Ymax-5:Ymax+5,Xmax-5:Xmax+5)=MHT_SNR(Ymax-5:Ymax+5,Xmax-5:Xmax+5);

%%%%%%%%%%%%%%%%%%%%%%%%%%%%%%%%%%%%%%%%%%%%%%%%%%%%%%%%%%%%%%%%%%

%centroid operation

xsum=sum(MHT_SNR1);

ysum=sum(MHT_SNR1');

H2sum=sum(sum(MHT_SNR1));


[y,x]=size(MHT_SNR1);


for k=1:x
    xprod(k)=xsum(k)*k;
end


for l=1:y
    yprod(l)=ysum(l)*l;
end


%%%%%%%%%%%%%%%%%%%%%%%%%%%%%%%%%%%%%%%%%%%%%%%%%%%%%%%%%%%%%%%%%%%%%%

%return position values

xpos=sum(xprod)/(2*H2sum)-5.5810;

ypos=sum(yprod)/(2*H2sum)-5.6550;
end
end
```

Bibliography

[1] "Aberrations". [Online.] Available: http://spie.org/x32395.xml.

[2] "SPACE SURVEILLANCE TELESCOPE (SST)". [Online.] Available: http://www.darpa.mil/Our˙Work/TTO/Programs/Space˙Surveillance˙Telescope˙(SST).aspx .

[3] "Zernike Polynomials". [Online.] Available: http://spie.org/x32527.xml.

[4] "Public Law 109-155–Dec. 30, 2005 119 STAT. 2895". *George E. Brown, Jr. Near-Earth Object Survey Act. 42 USC 16691*. United States Printing Office, 2005.

[5] Andrews, Larry C. and Ronald L. Phillips. *Laser Beam Propagation through Random Media*. SPIE, Bellingham, Washington, second edition, 2005.

[6] Bizouard, C. "Useful constants". [Online.] Available: http://hpiers.obspm.fr/eop-pc/models/constants.html .

[7] DARPA. "SST Australia: Signed, Sealed and Ready for Delivery", 2013. URL http://www.darpa.mil/NewsEvents/Releases/2013/12/06.aspx.

[8] Goodman, Joseph W. *Statistical Optics*. John Wiley and Sons, Inc., New York, 1985. ISBN 0-471-01502-4.

[9] Goodman, Joseph W. *Introduction to Fourier Optics, third edition*. Roberts and Company Publishers, Greenwood Village, CO, 2005.

[10] Jeon, Jae H. *Predicting the Performance of the Space Surveillance Telescope as a Function of Seeing Parameter*. Master's thesis, Air Force Institute of Technology, Wright-Patterson Air Force Base, Ohio, 3 2015.

[11] Maruskin, Jared M, Daniel J Scheeres, and Kyle T Alfriend. "Correlation of optical observations of objects in earth orbit". *Journal of Guidance, Control, and Dynamics*, 32(1):194–209, 2009.

[12] Noll, Robert J. "Zernike polynomials and atmospheric turbulence". *JOSA*, 66(3):207–211, 1976.

[13] Peterson, Curtis J. R. *Near Earth Object Detection Using a Poisson Statistical Model for Detection on Images Modeled From the Panoramic Survey Telescope and Rapid Response System*. Master's thesis, Air Force Institute of Technology, Wright-Patterson Air Force Base, Ohio, 3 2012.

[14] Pohlig, Stephen C. "An Algorithm for Detection of Moving Optical Targets". *Aerospace and Electronic Systems, IEEE Transactions on*, 25(1):56–63, 1989.

[15] Richmond, Richard D. and Stephen C. Cain. *Direct-Detection LADAR Systems*. SPIE, Bellingham, Washington, 2010. ISBN 978-0-8194-8072-9.

[16] Van Trees, Harry L. *Detection, Estimation, and Modulation Theory, Part I*. John Wiley and Sons, Inc., New York, 2001. ISBN 0-471-09517-6.

[17] Weeden, Brian, Paul Cefola, and Jaganath Sankaran. "Global Space Situational Awareness Sensors". *2010 Advanced Maui Optical and Space Surveillance Conference, Maui, Hawaii*. 2010.

[18] Wiesel, William E. *Modern Orbit Determination*. Aphelion Press, second edition, 2010.

[19] Woods, Deborah Freedman, Ronak Y. Shah, Julie A. Johnson, Alexander Szabo, Eric C. Pearce, Richard L. Lambour, and Walter J. Faccenda. "Space Surveillance Telescope: focus and alignment of a three mirror telescope". *Optical Engineering*, 52(5):053604–053604, 2013. URL http://dx.doi.org/10.1117/1.OE.52.5.053604.

[20] Zingarelli, J.C., Travis Blake, and Stephen Cain. "Improving Ground Based Telescope Focus Through Joint Parameter Estimation". *Advanced Maui Optical and Space Surveillance Technologies Conference, Maui, Hawaii*. 2012.

REPORT DOCUMENTATION PAGE

1. REPORT DATE *(DD–MM–YYYY)*	2. REPORT TYPE	3. DATES COVERED *(From — To)*
26–03–2015	Master's Thesis	Oct 2014–Mar 2015

4. TITLE AND SUBTITLE

Measuring Angular Rate of Celestial Objects Using the Space Surveillance Telescope

5a. CONTRACT NUMBER

5b. GRANT NUMBER

5c. PROGRAM ELEMENT NUMBER

6. AUTHOR(S)

Sligar, Anthony J., Captain, USAF

5d. PROJECT NUMBER

15G122

5e. TASK NUMBER

5f. WORK UNIT NUMBER

7. PERFORMING ORGANIZATION NAME(S) AND ADDRESS(ES)

Air Force Institute of Technology
Graduate School of Engineering and Management (AFIT/EN)
2950 Hobson Way
WPAFB, OH 45433-7765

8. PERFORMING ORGANIZATION REPORT NUMBER

AFIT-ENG-MS-15-M-019

9. SPONSORING / MONITORING AGENCY NAME(S) AND ADDRESS(ES)

Dr. Lindsay Millard
DEF ADVANCED RESEARCH PROJECTS AGCY (HR0011)
675 NORTH RANDOLPH STREET
ARLINGTON, VA 22203-2114, USA
(571) 218-4354, lmillard@rand.org

10. SPONSOR/MONITOR'S ACRONYM(S)

DARPA, TTO

11. SPONSOR/MONITOR'S REPORT NUMBER(S)

12. DISTRIBUTION / AVAILABILITY STATEMENT

DISTRIBUTION STATEMENT A:
APPROVED FOR PUBLIC RELEASE; DISTRIBUTION UNLIMITED

13. SUPPLEMENTARY NOTES

This work is declared a work of the U.S. Government and is not subject to copyright protection in the United States.

14. ABSTRACT

To date, much effort has been spent on improving the detection of space objects; however, the ability to track and catalogue space objects remains only as good as the ability to determine the object's position and angular rate. The foundation of space situational awareness (SSA) is the ability to detect a space object and to predict its location in the future. In order to accomplish SSA for Geosynchronous Earth Orbit (GEO) space objects, the Defense Advanced Research Projects Agency (DARPA) developed the Space Surveillance Telescope (SST) to enable ground-based, broad-area search, detection and tracking of small GEO objects in space. In general, the SST tracks along the sky at the sidereal rate where the stars will appear to be stationary, while objects within space not moving at this rate will appear to move across the focal array from data frame to data frame. As the time between each frame is known and the position of the detected object can be determined in the focal array, it is possible to measure the angular position and angular rate of a detected object. The two main types of detection algorithms used in this thesis are the binary hypothesis test (BHT) and the multi-hypothesis test (MHT), which both rely on a log-likelihood ratio (LLR); however, the MHT algorithm adds an additional step to correlate nine system point spread functions, or hypotheses, with the image data. These detection algorithms lead to varying degrees of accuracy and precision in determining the position and angular rate for a detected space object. The research within this thesis shows that the MHT algorithm is more accurate and precise than the BHT algorithm.

15. SUBJECT TERMS

detection theory, Fourier optics, angular rate, signal processing, statistical optics

16. SECURITY CLASSIFICATION OF:			17. LIMITATION OF ABSTRACT	18. NUMBER OF PAGES	19a. NAME OF RESPONSIBLE PERSON
a. REPORT	b. ABSTRACT	c. THIS PAGE			Stephen C. Cain, PhD (ENG)
U	U	U	UU	101	**19b. TELEPHONE NUMBER** *(include area code)* (937) 255-3636 x4716 Stephen.Cain@afit.edu